~~The influence of~~ Strike-slip faulting affecting vertical ~~lithological contrasts on strike-slip fault behavior~~domains of contrasting brittle strength in the upper crust: Insights from analogue models.

Sandra González-Muñoz[1], Guido Schreurs[2], Timothy C. Schmid[2], Fidel Martín-González[1]

[1]Área de Geología - ESCET, TECVOLRISK Research Group, Universidad Rey Juan Carlos. C/Tulipan s/n, Mostoles, 28933 Madrid, Spain
[2] Institute of Geological Sciences, University of Bern, Bern, Switzerland

Correspondence to: Sandra González Muñoz (sandra.gonzalezmu@urjc.es)

Abstract

~~This work investigates the influence of rheological contrasts on the nucleation and behavior of strike-slip faults. To achieve this, we have carried out a series of brittle-viscous strike-slip shear analogue models, using quartz sand and microbeads as granular materials with different internal friction and cohesion values. Particle Imaging Velocimetry (PIV) was applied to time-series of surface images to calculate incremental and cumulative strains. Understanding how strike-slip faults nucleate and interact in the heterogeneous upper crust is relevant in seismic hazard analysis and geothermal and hydrocarbon exploration. To reproduce the heterogeneity of the upper crust, three sets of experiments we performed: 1) upper layer composed either of quartz sand or microbeads; 2) upper layer with a vertical contrast i.e., quartz sand surrounded by microbeads and vice-versa; and 3) same set-up as in the previous set but changing the orientation of the vertical contrast. Our study shows that the introduction of an upper crustal vertical contrast influences the behavior and evolution of strike-slip faults. The models containing a vertical contrast were more complex and induced a compartmentalization of the model. The initial fault strike is related to the material's properties. However, this initial strike changes when faults crosscut the materials with less~~

Definición de estilo: Normal
Definición de estilo: Revisión: Inglés (Reino Unido)

internal friction angle clockwise, and anticlockwise when the contrast has higher internal friction angle. Areas containing materials with less internal friction angle take longer to localized the deformation, but they show a greater number of faults. The biggest increase in the number of synthetic and antithetic faults occurs with the introduction of vertical contrast. These results were compared with the intraplate fault systems of the NW Iberian Peninsula, focusing on the Penacova-Régua-Verin and Manteigas-Vilariça-Bragança fault systems. They are major left-lateral faults that cross-cut lithologies characterized by vertical rheological contrasts, with deformation patterns similar to those observed in our analogue models.

This study investigates how strike-slip faults propagate across vertical domains of contrasting brittle strength using analogue models. Strike-slip faults are long structures that cut across pre-existing tectonic or lithological steep boundaries in the upper crust. The interaction between strike-slip faulting and these domains is crucial for understanding the evolution of regional and local fault patterns, potential stress reorientations, and seismic hazard assessment. Our models undergo sinistral distributed strike-slip shear (simple shear) and comprise brittle vertical domains with contrasting properties. We use quartz sand and microbeads as brittle analogue materials over a viscous mixture to distribute the deformation through the model. We apply Particle Imaging Velocimetry (PIV) and use incremental vorticity to analyse models surfaces. The first models investigate strike-slip fault kinematics with only one brittle material (quartz sand or microbeads), simulating a homogeneous crust. Three further models examine how the orientation of a central vertical domain, having a strength contrast with respect to the surrounding domains, influences strike-slip faulting. The main observations of this study are the following:

- The presence of vertical domains of contrasting brittle mechanical strength has a profound effect on synthetic fault propagation, interaction and linkage as well as the kinematic evolution of antithetic faults that rotate about a vertical axis due to the applied simple shear.
- The orientation of the central domain determines whether antithetic fault activity concentrates along the entire width of the domain boundaries or not. In the first case, fault activity is compartmentalized in distinct domains. In the second case (no or partial fault activity along domain boundaries), the relative brittle strength contrast determines fault propagation, interaction and/or linkage across the central domain.

These findings were compared with the intraplate fault systems of the NW Iberian Peninsula, which shows synthetic and antithetic faults whose distribution is similar to those observed in our models.

Keywords

Strike-slip fault zone, Fault ~~segmentation, Rheological~~interaction, Fault linkage, Vertical brittle strength contrasts, Analogue modelling

1. Introduction

The structural styles and the factors that control the geometry of strike-slip faults have been investigated in detail in many studies (e.g~~.~~., Riedel, 1929; Anderson, 1951; Deng et al., 1986; Sylvester, 1988; Dooley and Schreurs, 2012; Hatem et al., 2017; Lefevre et al., 2020a; Visage et al., 2023). In nature, strike-slip fault systems typically have complex architectures consisting of numerous segments separated by steps or of anastomosing, linked fault zones (e.g., Aydin and Nur, 1982; Barka and Kadinsky-Cade, 1988; Wesnousky, 1988; Stirling et al., 1996; Kim et al., 2004). How faults interact or link is considered to be a function of loading, stress disturbances, rheology and the geometry of pre-existing structures (e.g., Kim et al., 2004; Myers and Aydin, 2004; Peacock and Sanderson, 1991, 1992; Burgmann and Pollard, 1994; Sibson, 1985; Gamond, 1983; Rispoli, 1981; Wesnousky, 1988).

Understanding strike-slip fault interaction and linkage is important not only in view of the location of geothermal and hydrocarbon resources (e.g. Sibson, 1985; Martel and Peterson, 1991; Aydin, 2000; Odling et al., 2004; Cazarin et al., 2021) but also for its implications on regional stress orientations (Kirkland et al., 2008), as well as seismic hazard (Petersen et al., 2011; Bullock et al., 2014), in terms of dynamics, fault growth and size of earthquakes (e.g. Aki, 1989; Harris and Day, 1999; Scholz, 2002; Wesnousky, 2006; Shaw and Dieterich, 2007; de Joussineau and Aydin, 2009; Preuss et al., 2019).

Various studies have investigated the influence of vertical changes in mechanical strength (e.g., a horizontal ~~rheological contrasts (e.g., mechanical stratigraphy of~~ sedimentary ~~sequences~~sequence comprising layers or bodies of different strengths) on strike-slip fault orientation, segmentation, linkage, and displacement, using field observations ~~(e.g., Peacock and Sanderson, 1992), combining,~~ combined with analytical and numerical methods (e.g. Du and Aydin, 1995; Aydin and Berryman, 2010; De Dontney et al., 2011), ~~and~~or analogue models (Richard, 1991; Richard et al., 1995; Gomes et al., 2019; Gabrielsen et al., 2023; Venancio and Alves Da Silva, 2023). However, only the study from Gomes et al (2019) has investigated systematically the influence of vertical rheological contrast in strike slip fault behavior, using silicone as weak body immersed in between the horizontal layers of the model. The strike slip fault behaviour trough changes in the rheological properties of the upper crust is of particular importance in the context of strike-slip fault zones. As a consequence of their long

Strike-slip fault systems have large aspect ratios (i.e., ratio (i.e. ratioof length vs width), they) and can extend over hundreds or even thousands of kilometres and often cut across pre-existing tectonic contacts with or lithological boundaries that are steeply oriented and have rocks of contrasting rheologies.mechanical strength on either side. Hence, it is also important to understand the interaction between vertical domains of contrasting mechanical strength and strike-slip faulting. To our knowledge no modelling studies have systematically investigated how strike-slip fault systems are influenced by pre-existing steeply oriented domains with rocks of contrasting mechanical strength on either side of the contacts. Such (sub)vertical contacts often occur at crustal terrane boundaries, but also occur within crustal blocks comprising rock units of contrasting strength separated by vertical boundaries, e.g. a magmatic body with steep margins that intruded into a sedimentary sequence.

Con formato: Sin Resaltar

In this study,Here we use scaled analogue model experiments analysed by PIV to assess the role of vertical rheological contrastsdomains of contrasting brittle strength in the upper crust on fault kinematics in distributed strike-slip shear. TheOur results obtained show howthat the presence of such vertical contrast influencesdomains with different strengths has a profound influence on the orientation,kinematic evolution and number of faults. The obtainedstrike-slip fault systems. We compare our experimental model results are compared with one naturala crustal-scale example in the NW part of the Iberian Peninsula, where two large parallel strike-slipand sinistral strike-slip fault systems cut lithologies withlithological domains of contrasting brittle rheologiesstrength.

2. Methods

2.1. Analogue model setup and monitoring

In this study, eight simple shear experiments are presented. The experimental machine comprisesset-up for simulating distributed strike-slip shear included a mobile base plate that cancould be translated horizontally alongpast a fixed base plate (Fig. 1). An assemblage of 60 individual and moveable plexiglass bars (each 7978 cm long, 5 cm high and 5 mm wide) overlies the was positioned on top of two base plates, which are . The assemblage of plexiglass bars was confined by two longitudinal carbon-fiber sidewalls on the long sides (Fig. 1b) and twowooden bars (c. 5 mm high, 2 cm wide and 40 cm long) on the short sides (Fig. 1b, c), that could pivot below the longitudinal sidewalls consisting of vertical rubber sheets.. The analogue model iswas constructed on top of the plexiglass bars and consistsconsisted of a 2 cm-thick viscous layer and a 2 cm-thick brittle layer, , simulating the ductile lower crust, overlain by a 2 cm-thick layer of granular materials simulating the brittle upper crust. The short sides of the model were confined by vertical rubber sheets. Although our model set-up thus included both a horizontal viscous layer overlain by a horizontal brittle layer, our experiments focus on the influence of vertical domains with brittle strength contrasts on strike-slip faulting. The function of the viscous layer, directly overlying the plexiglass bars, is to simulate the lower distribute the applied shear deformation over the entire width of the model in the overlying brittle layer (e.g. Schreurs, 1991, 2003; Dooley and upper crust respectively. In this way, we avoid the possible boundary effects due to the interaction between the brittle materialsSchreurs, 2012).

Each model had an initial rectangular shape in map view, with a length of 78 cm parallel to the shear direction and the plexiglass bars. Initially, the horizontal model dimensions in each model are 78 cm x a width of 30 cm. perpendicular to it. The movement of the mobile base plate occurred by computer-controlled stepper motors providingat a constant velocity of 40 mm/h in all experiments, obtaining, resulting in 80 mm of total displacement after two hours. Displacement of the mobile base plate changed the initial rectangular shape of the overlying assemblage of plexiglass bars into a parallelogram simulating simple shear.

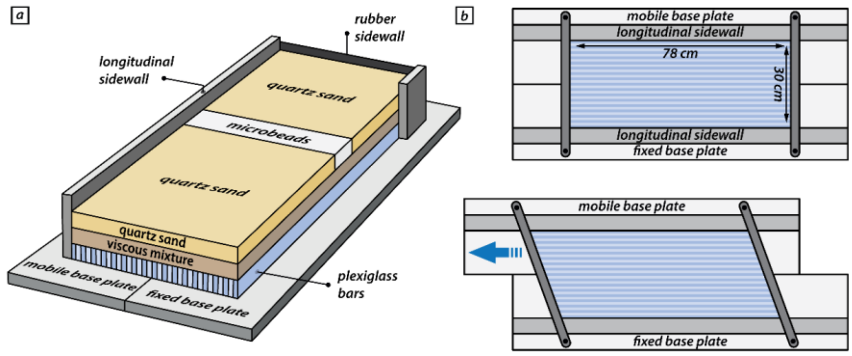

Figure 1: Schematic experimental setup. (a) The base of the model set-up consists of a fixed plate and a mobile plate overlain by an assemblage of individual and moveable plexiglass bars. The model is constructed on top of the plexiglass bars and is confined by two longitudinal sidewalls and two short sidewalls consisting of rubber sheets. (b) upper panel: Initial position of base plates overlain by plexiglass bars confined on the short sides by wooden bars that can pivot about a vertical axis; lower panel: Sinistral horizontal displacement of the ~~basal~~ mobile base plate ~~results in~~induces a ~~distributed sinistral strike-slip~~simple shear movement in the overlying ~~model materials. The systematics followed throughout this work includes~~assemblage of plexiglass bars as they slide past one another.

We performed four series of simple shear experiments ~~(Fig. 2;~~, referred to as Series A, B, C and D (Fig. 2). Series A involved two reference models with only one brittle material (Fig. ~~3a~~2a), either quartz sand or microbeads ~~(MB),~~, to investigate strike-slip fault kinematics in ~~models~~ a homogeneous upper crust, without any ~~vertical rheological contrast. The following~~lateral variations in mechanical strength. In the subsequent three series ~~simulated vertical rheological contrasts by adding a c. 5 cm wide central band composed~~(Fig. 2b-d), we introduced vertical domains that consisted of quartz sand ~~with microbeads~~or microbeads. Each model had three domains with a c 5-cm-wide central domain consisting of a different brittle material than the domains on either side ~~or vice versa (Fig. 2;~~ . The difference between Series B, C~~, and D). Two~~ and D is the orientation of the central domain with respect to the shear direction, which changed from one series to the next. To achieve such a model set-up, two vertical thin sheets of cardboard (< 1 mm) were first placed as provisional walls, spaced 5 cm apart, on top of the viscous layer in the central domain of the model~~.~~, parallel to the required orientation of the vertical boundaries. Subsequently, the different granular materials were sieved on top of the viscous layer and once the desired model thickness was reached, the cardboard sheets were carefully removed. ~~Hence, we obtained two vertical rheological contrasts that consist of reactivated lithological boundaries.~~ Although removal of the cardboard produced increased dilation

Con formato: Fuente: 9 pto, Negrita
Con formato: Fuente: 9 pto, Negrita
Con formato: Fuente: 9 pto, Negrita
Con formato: Fuente: 9 pto, Negrita
Con formato: Fuente: 9 pto, Negrita
Con formato: Fuente: 9 pto, Negrita

along a narrow zone, it hardly affects the de facto function of this vertical boundary as a primary surface with materials of contrasting brittle strength on either side. For descriptive purposes, we ~~assign a N orientation~~ defined a North direction, which is perpendicular to the applied shear direction and parallel to the short sides of the undeformed model. ~~Considering this, three different vertical contrast orientations were tested: N-S (Series B), N20°W (Series C), and N20°E (Series D). With the addition of the central~~ (Fig. 2a). In models with a brittle strength contrast, we can distinguish ~~three~~two outer domains ~~in our model descriptions: a~~ , a western ~~domain, a central domain (i.e., the band of contrasting material), and~~ and an eastern one, and a central domain~~.~~ (Fig. 2b-d).

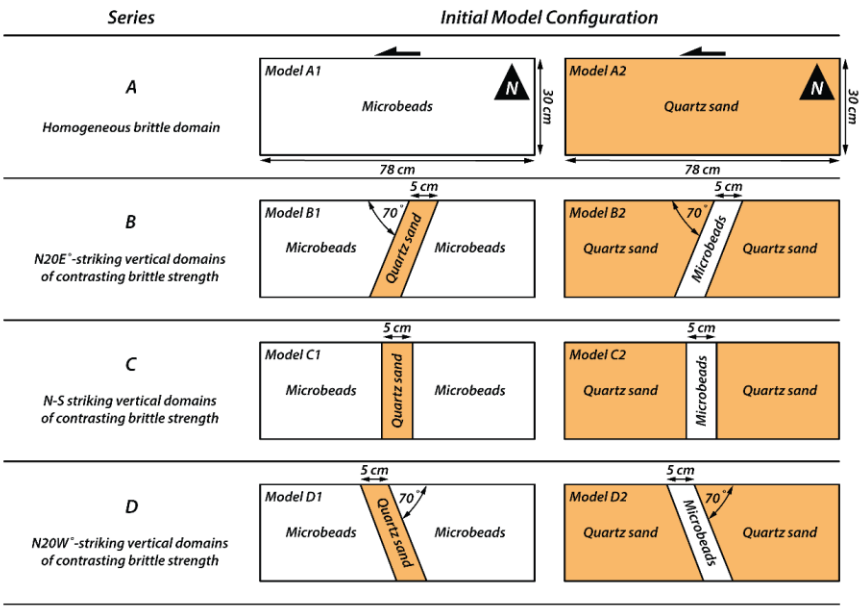

Figure 2: Schematic top views of the four series of models, with dimensions and brittle analogue materials used

2.2. Analogue materials

We used two different types of granular materials in our analogue models to assess the role of vertical zones of contrasting mechanical strength in the upper crust: quartz sand and microbeads grains. The quartz sand (distributor Carlo Bernasconi AG; www.carloag.ch) has a grain size between 60 and 250 µm with a bulk

Con formato: Inglés (Estados Unidos)

Con formato: Fuente: Negrita, Inglés (Reino Unido) density of 1560 kg m^{-3}, whereas the grain size of the microbeads (distributor: Worf Glasskugeln, Germany) lies between 150 and 210 µm with a bulk density of 1400 kg m^{-3}. These density values were achieved by sieving the granular material into the model box from a height of 30 cm. Both, quartz sand and microbeads deform according to the Coulomb failure criterion and have internal peak friction angles of 36° and 22° and cohesion values of 50 ± 26 Pa and 25 ± 4 Pa, respectively (Panien et al., 2016; Schmid et al., 2020). The considerable difference in the internal peak friction angle between the two materials makes them suitable for simulating contrasting upper crustal rocks. According to their difference in the internal friction angle, we consider the microbeads and quartz sand as weak and strong materials, respectively.

The viscous layer in our models had a density of 1600 kgm^{-3} and consisted of a mixture of SGM-36 polydimethylsiloxane (PDMS) and corundum sand (weight ratio of 0.965: 1.000). The mixture has a quasi-linear viscosity of 1.5 ×10^{5} Pa s and a stress exponent of 1.05 (Zwaan et al.,

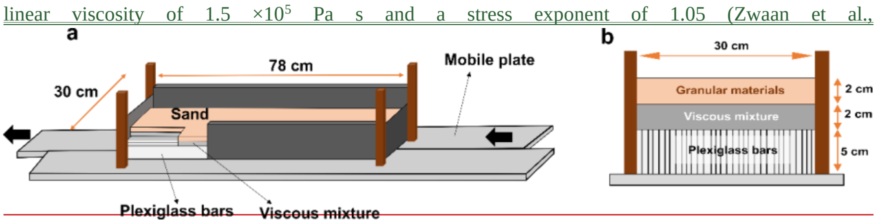

Figure 1: Experimental setup for conducted experiments. A) Schematic representation of the sandbox. The base of the model set-up consists of a fixed plate and a mobile wall. The model is confined by two short sidewalls, consisting of rubber sheets and two long sidewalls. B) Model setup cross sections, showing the assemblage of plexiglass bars below the model materials.

2018). The properties of all analogue materials are summarized in Table 1.

Granular materials	Quartz sand	Microbeads	Viscous material	PDMS/corundum mixture
Density (kg/m^3)	1560	1400	Density (kg/m^3)	1600
Grain size (µm)	60-250	150-210	Viscosity (Pa s)	1.5x10^5
Peak friction coefficient µ and angle, ϕ	0.72 - 36°	0.41 - 22°	Stress exponent n	1.05

Cohesion (Pa)	50 ± 26	25 ± 4

Table 1: Materials properties of used granular and viscous materials (after Panien et al., 2006; Schmid et al., 2020).

2.3. Scaling

For brittle Mohr-Coulomb type materials, dynamic similarity is given by the equation for stress ratios

$$\sigma^* = \rho^* g^* h^* \quad (1),$$

where ρ^*, g^* and h^* are the ratios of model to nature for density, gravity and length, respectively. Note, that our two used granular materials have different densities, cohesions and internal friction coefficients. However, the resulting scaling factors are nearly identical and therefore we provide only the scaling factors for quartz sand. Where scaling factors substantially differ, we denote them with subscripts "qtz" and "mb" for quartz sand and microbeads, respectively. Our model setup yields a length scaling factor of $h^* = 2 \times 10^{-6}$ and a gravity scaling factor of 1. For quartz sand, the density scaling factor is $\rho^*_{qtz} \sim 0.6$ and the cohesion factor is $C^*_{qtz} = 1 \times 10^{-6}$ (using a cohesion of ~50 Pa and 50 MPa for our quartz sand and upper crustal rocks, respectively; Byerlee, 1978). Additionally, for microbeads the density scaling factor and cohesion scaling factor are $\rho^*_{mb} \sim 0.5$ and $C^*_{mb} = 1 \times 10^{-6}$ (assuming a weakened natural rock type with a cohesion of c. 25 MPA), respectively. Using these scaling factors yields a stress scaling factor of $\sigma^* = 1 \times 10^{-6}$ for both quartz sand and microbeads.

Assuming a lower crustal viscosity of $\eta = 10^{22}$ Pa s (Moore and Parsons, 2015; Zhang and Sagiya, 2017) yields a viscosity ratio $\eta^* = 1 * 10^{-17}$ (using the viscosity of $1.5 * 10^5$ Pa s for the viscous analogue material).

The strain rate ratio is obtained from the stress ratio and the viscosity ratio by (Weijermars and Schmeling, 1986):

$$\dot{\varepsilon}^* = \frac{\sigma^*}{\eta^*} \quad (2).$$

Note that due to the simple shear setup, we substitute the strain rate scaling factor $\dot{\varepsilon}^*$ with the shear strain rate scaling factor $\dot{\gamma}^* = 1 \times 10^{11}$. Next, the velocity scaling factor v^* and a time scaling factor t^* are calculated with

$$\dot{\gamma}^* = \frac{v^*}{h^*} = \frac{1}{t^*} \quad (3)$$

yielding a velocity scaling factor $v^* = 2 \times 10^5$ and a time scaling factor $t^* = 1 \times 10^{-11}$.

Based on our scaling, 1 cm in our experiments corresponds to 5 km in nature and the applied velocity of 40 mm h^{-1} converts to a velocity of ~2 mm a^{-1} in nature. Using the shear strain rate scaling factor $\dot{\gamma}^*$, the bulk shear strain rate $\dot{\gamma} = 3.7 \times 10^{-5}\ s^{-1}$ in our models translates to a shear strain rate of $\dot{\gamma} = 3.7 \times 10^{-16}\ s^{-1}$ in nature and 1 h in our analogue experiments translates to ~12.5 Myr in nature.

In order to verify dynamic similarity of brittle natural and experimental material we calculate the Smoluchowski number S_m, which is the ratio between gravitational stress and cohesive strength (Ramberg, 1981):

$$S_m = \frac{\rho g h}{C + \mu \rho g h} \quad (4),$$

where ρ, h, C and μ are the density, thickness, cohesion, and friction coefficient, respectively of the brittle material. With a cohesion of 50 MPa and a friction coefficient of ~0.6 (Byerlee, 1978) for upper crustal rocks, this yields values of $S_m \sim 1$ for our models as well as for nature. We further calculate the Ramberg number R_m to ensure dynamic and kinematic similarities between the viscous layers.

$$R_m = \frac{\rho g h^2}{\eta v} \quad (5)$$

For our velocity of 40 mm h^{-1}, this yields a Ramberg number of 6 for both, our models and nature. The Reynolds number R_e is defined as the ratio between inertial forces and viscous forces and is for all our models as well as for the natural prototype << 1:

$$R_e = \frac{\rho v h}{\eta} \quad (6)$$

Based on the applied scaling laws, the material properties and the similar non-dimensional numbers for model and nature, we consider our models to be properly dynamically scaled. Model parameters and dynamic numbers of the used materials are specified in Table 2.

	General parameters			Brittle upper crust		Ductile lower crust		Dimensionless numbers		
	Gravity [m/s²]	Crustal thickness [m]	Shear velocity [m/s]	Density [kg/m³]	Cohesion [Pa]	Density [kg/m³]	Viscosity [Pa s]	Smoluchowski Sm	Ramberg Rm[1]	Reynolds Re
Model	9.81	4×10^{-2}	1.1×10^{-6}	1560	50	1600	1.5×10^{5}	1	6	<<1
Nature	9.81	2×10^{4}	6.3×10^{-11}	2700	5×10^{7}	2900	1×10^{22}	1	6	<<1
Scaling ratios $x^* = x^m/x^n$ [dimensionless]										
	σ^*	ρ^*	g^*	h^*	C^*	$\dot{\gamma}^*$	η^*	v^*	t^*	
	1×10^{-6}	0.5[1]-0.6	1	2×10^{-6}	5[1]-10 x 10^{-7}	1×10^{11}	1×10^{-17}	2×10^{5}	1×10^{-11}	

[1] Lower values for scaling factors ρ^* and C^* refer to microbeads.

Table 2: Scaling parameters and scaling factors.

2.4. Deformation monitoring and quantification

Since the experiments were conducted using a simple shear setup, vertical motions during deformation were negligible, with nearly all movement located within the horizontal plane. The different experiments were monitored by an automated Nikon D810 (36 MPx) DSLR camera positioned above the experimental model. Images were taken at fixed intervals of ~~30 sec~~60 s during two hours, resulting in ~~240 pictures in total~~121 subsequent top view images of the model surface. For a quantitative 2D analysis of the surface deformation, we used the StrainMaster module of the LaVision© DaVis image correlation software. ~~This software allows us to do the camera~~ Using a calibration~~,~~ plate, the software corrects the ~~mapping~~top view images for lens distortion effects (i.e., unwarping), applies image rectification and provides a scaling function ~~for~~ that maps coordinates from the camera sensor to physical world coordinates with a resolution of ~9 px/mm. The digital image correlation~~, and the~~ calculates local displacement ~~calculation by~~vectors on subsequent images using a square matching algorithm with adaptive multi-pass cross-correlation. ~~We use~~To properly track freckle patterns, we sprinkled coffee grains on the model surface prior to the model run. For each image, the analyzed area is subdivided into small interrogation window for which a local displacement vector is determined by cross-correlation. We used subsets (i.e., interrogation windows) of 31 by 31 pixels with a 75% overlap for the local displacement calculations~~. The pictures obtained have an average area of 8256 by 5504 pixels for the X~~ that, assembled result in incremental (60 s interval) displacement fields for the horizontal x- and ~~Y axis~~y-components u_x and u_y, respectively~~,~~ with ~~an average~~a vector resolution of ~~300 pixels~~~1.3 vectors/mm.

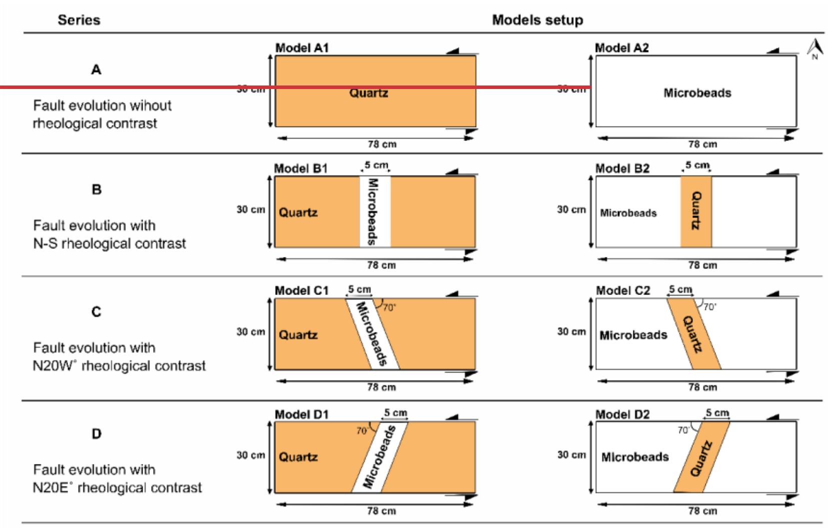

~~**Figure 2: Schematic top views of the four series of models, with dimensions and materials used in each series.**~~

~~Since the experiments were conducted using a simple shear setup (see Fig. 1a), vertical motions during deformation were negligible, with all the movement located within the horizontal plane. The quantitative deformation analysis included: (1) scaling and rectifying top view images; (2) subsequent displacement calculation and; (3) the application of statistical analysis representing the dominant fault orientations, measured every 2 cm, in rose diagrams. The DaVis software calculates incremental displacement fields based on a direct correlation algorithm and provides access to individual displacement components. We used~~Postprocessing included an outlier filter to fill gaps of pixels within a 3 by 3 neighborhood (Westerweel and Scarano, 2005). Discarded vectors in the displacement fields were replaced by an iterative interpolation requiring at least two neighboring vectors. For quantifying deformation at the model surface, we calculate the z-vorticity ω_z (i.e., a local measure of rotation within the xy-plane) as a proxy for shear movement along strike-slip faults. In contrast to the shear strain ε_{xy}, vorticity is not dependent on the orientation of the coordinate system, which is crucial when quantifying deformation along faults that strike obliquely with respect to the coordinate system (e.g., Cooke et al., 2020). ω_z can be derived from local displacement gradients according to equation 1:

$$\omega_z = \frac{\partial v}{\partial x}\frac{\partial u_y}{\partial x} - \frac{\partial u}{\partial y}\frac{\partial u_x}{\partial y} \qquad (17)$$

Tabla con formato

With uu$_x$ and vu$_y$ being the horizontal displacement components in the x, and y direction, respectively. Due to convention, positive and negative ω_z values refer to sinistral and dextral shear sense, respectively. Postprocessing includes an outlier filter to fill gaps of pixels within a 3 by 3 neighbourhood (Westerweel and Scarano, 2005). Discarded vectors in the displacement fields are replaced by an iterative interpolation requiring at least two neighboring vectors. When summing up incremental displacement fields, flow advection due to applied velocities are considered using the Lagrangian sum of displacements (Boutelier et al., relative displacement, respectively. Within the predefined increment of 60 s, ω_z values are consistently within the range [-2%, 2%] and we set a threshold of -0.5% and 0.5% to distinguish between active deformation and background noise for dextral and sinistral shear sense, respectively. In the results section we present ω_z at deformation stages every 30 min (i.e., after 30, 60, 90, and 120 min). Finite deformation after 120 min for each model is illustrated with a surface photograph and enhanced with superposed line drawings of the fault pattern. For the statistical analysis of fault orientations, we traced active fault segments (i.e., $\omega_z \leq$ -0.5 % or $\omega_z \geq$ 0.5 %) in MATLAB using polylines, where each fault segment is defined by two consecutive vertices. At each time step, segment length and azimuth were calculated and visualized in length-weighted rose diagrams.2019). We determined incremental and cumulative vorticity for each time step, i.e., at every 30 seconds.

Con formato: Fuente: Negrita, Inglés (Reino Unido)

2.2.1.1. Analogue materials

We use two different types of granular materials in our analogue models to assess the role of vertical rheological contrasts in the upper crust: quartz sand and microbeads grains. The quartz sand (distributor

Carlo Bernasconi AG; www.carloag.ch) has a grain size between 60 and 250 µm, whereas the grain size of the microbeads (distributor: Worf Glasskugeln, Germany) lies between 150 and 210 µm. Quartz sand and microbeads deform according to the Coulomb failure criterion and have internal peak friction angles of 36° and 22° and cohesion values of 48 ± 26 Pa and 25 ± 4 Pa, respectively (Panien et al., 2016; Zwaan et al., 2018c; Schmid, 2023). The considerable difference in the internal peak friction angle between the two materials makes them suitable for simulating contrasting upper crustal, brittle rheology. Considering their differences between their internal friction angle, we are going to assume through the entire manuscript that the microbeads and quartz sand are weak and strong materials respectively.

The granular materials are sieved on top of a viscous layer representing the lower ductile crust (Fig. 1b). This viscous layer, placed directly on top of the plexiglass bars, consists of a mixture of SGM-36 polydimethylsiloxane (PDMS) and corundum sand (weight ratio of 0.965: 1.000), which has a density of 1600 kgm^{-3}. The mixture has a quasi-linear viscosity of 1.5×10^5 Pa s and a stress exponent of 1.05 (Zwaan et al., 2018c). The properties of all materials are summarized in Table 1.

Granular materials	Quartz sand	Microbeads
Density ρ (kg/m3)	1560	2300
Grain size (µm)	60-250	150-210
Friction coefficient µ	0,72	0,41
Angle of internal Friction °	36°	22,3°
Dynamic stable friction	31,4°	20,6°
Reactivation friction angle (ϕp)	33,4°	21,9°
Cohesion (Pa)	48+-26	25+-4
Viscous mixture	**PDMS**	
Density (Kg/m^3)	1600	
Viscosity η (Pa·s)	150000	

Table 1: Materials properties. For properties of microbeads (Panien et al 2006., Zwaan et al., 2022; Schmid et al., 2022) Viscous mixture: Polydimethylsiloxane (PDMS) mixed with corundum sand; 1:1 weight ratio.

2.3. Scaling

The scaling of the models is based on Hubbert (1937) and Ramberg (1981). The brittle materials are scaled using the dynamic similarity equation obtained from the scale's ratios (equation 2). Where ρ^*, g^*, h^* and η^* are the density, gravity, length, and viscosity. The asterisk indicates the ratio of model to nature for that component. The stress ratio is approximately $\sigma^* = 1.13\times10^{-6}$, with 1 cm in the models representing 5 km in nature (Table 2).

$$\sigma^*=\rho^*g^*h^* \quad (2)$$

~~Assuming a lower crustal viscosity of η = 10^22 Pa s (Moore and Parsons, 2015; Zhang and Sagiya, 2017) yields a viscosity scaling ratio η* = 10^−17, which gives 1.13x10^11 for the strain rate ratio (ε*) calculated with equation 3, which correlates the stress ratio (σ*) and the viscosity ratio (η*).~~

$$\varepsilon^* = \sigma^*/\eta^* \qquad (3)$$

~~In order to verify that the dynamic similarities in the models, the Smoluchowski (S_m) and Ramberg (R_m) numbers were determined. The first one (Equation 4) describes the ratio between gravitational stress and cohesive strength (Ramberg, 1981). Where ρ, h, C and μ are the density, thickness, cohesion and friction coefficient, respectively. The second, R_m, describes the ratio between gravitational and viscous stresses (Equation 5; Ramberg, 1981). Model parameters and non-dimensional numbers are given in Table 2.~~

$$Sm = \rho g h / C + \mu \rho g h \qquad (4)$$

$$Rm = \rho g h^2 / \eta v \qquad (5)$$

	General parameters			Brittle upper crust		Ductile lower crust		Smoluchowski (Sm)	Ramberg (Rm)	Reynolds (Re)
	Gravity (m/s2)	Thickness h (m)	Velocity (m s− 1)	Density ρ (kg/m3)	Cohesion (Pa)	Density ρ (kg/m3)	Viscosity η (Pa·s)			
Model	9,81	4,00E-02	2,80E-06	1560	50,00	1600	1,00E+05	1	22	<<1
Nature	9,81	2,00E+04	1,23E-11	2750	5,00E+07	2900	1,00E+22	1	20	<<1
	σ*	ρ*	g*	h*	c*	Ɛ*	η*	v*	t*	
	1,13E-06	0,57	1,00E+00	2,00E-06	1,20E+00	1,13E+11	1,00E-17	2,27E+05	8,81E-12	

~~**Table 2: Scaling parameters and scaling ratios for the reference model Setup with a Brittle Ductile Thickness Ratio T_{BD} = 1**~~

3. Results

~~3.1. Series A. Fault evolution without vertical rheological contrast~~

We present the results of eight distributed strike-slip shear experiments, grouped in four series of two models each. Series A models included two reference models having a homogeneous upper brittle layer, whereas Series B, C and D models had vertical domains with contrasting brittle strengths (Fig. 2).

Con formato: Fuente: 10 pto, Inglés (Reino Unido)

Con formato: Justificado, Espacio Antes: 12 pto, Interlineado: Doble

3.1. Series A: Fault evolution in a homogeneous upper crust

The Series A models ~~consist~~consisted of a homogeneous upper crustal layer composed of ~~a brittle layer of~~ either microbeads (Fig. 3; Model A1) or quartz sand (Fig. ~~3; Model A1) or microbeads (Fig.~~ 3; Model A2). The incremental strain panels document that strain ~~localizes~~localized first in the model with quartz sand, while deformation ~~is~~was still diffuse in the model with microbeads (Fig. 3a and f~~).~~), i.e. strain localization occurs at lower amounts of applied simple shear in quartz sand than in microbeads. With ~~increasing~~progressive sinistral simple shear deformation, slightly overlapping right-stepping *en echelon* strike-slip faults with a sinistral ~~strike-slip~~ displacement ~~form~~formed (Fig. 3b and g). These faults were synthetic with respect to the bulk simple shear. In the ~~experiment~~model with ~~quartz sand~~microbeads (Model A1) the first synthetic faults ~~to form strike N70°E~~had an orientation of c. N79˚E (Fig. 3b), whereas ~~the initial faults~~ in the ~~experiment~~model with ~~microbeads~~quartz sand (Model A2) ~~strike N80˚E~~their orientation was c. N72˚E (Fig. 3g). Initial deformation in both models is accommodated ~~only~~ by synthetic (sinistral) strike-slip faults only (Fig. 3a, b and f, g). As deformation ~~progresses~~progressed, individual fault segments ~~link~~linked up ~~to form through-going~~forming major sinistral strike-slip faults (Fig 3c and h). Antithetic faults only developed in Model A2 (quartz sand only; Fig. 3h and i) at later stages of deformation. These faults were confined in between previously formed synthetic faults. The final deformation stage (Fig. 3e and j) shows that most deformation was taken up by major synthetic faults that crossed the entire length of the model. At the final stage, the initial *en echelon* pattern of faulting was better preserved in the quartz sand model than in the microbeads model, resulting in a wider damage zone in the former.

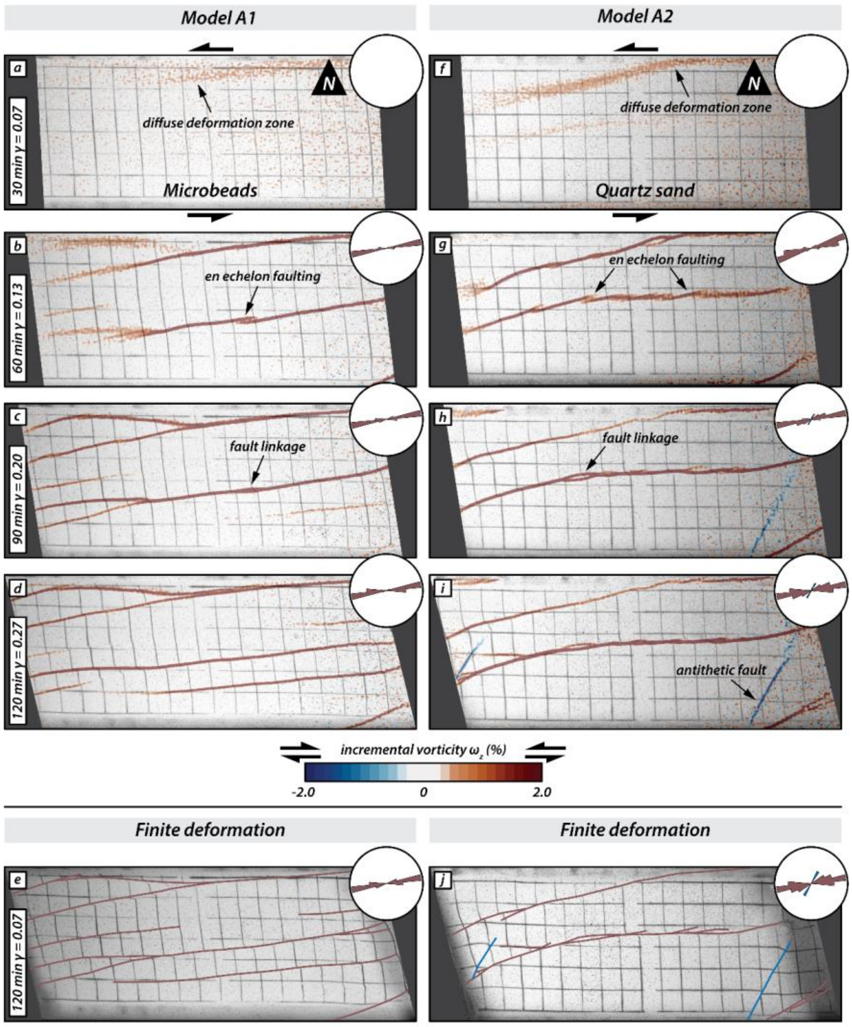

Figure 3: Overview of Series A models: Simple shear deformation of two models with a homogenous upper brittle layer. The first four panels of each series show surface photographs with the incremental vorticity after 30 minutes (20 mm displacement of mobile base plate), 60 minutes (or 40 mm displacement), 90 minutes (or 60 mm displacement) and 120 minutes (or 80 mm displacement). Incremental positive and negative values indicate sinistral (synthetic, red) and dextral (antithetic, blue) relative movement, respectively. The last panel for each series shows a surface photograph of the final stage overlain with the interpreted fault pattern; red lines are sinistral faults, blue lines are dextral faults.

3.2. Series B: Fault evolution in models with N20°E vertical domain boundaries

The vertical domain boundaries in the Series B models were oriented N20°E. Model B1 had a central domain consisting of strong quartz sand with weak microbeads in the adjacent, western and eastern domains (Fig. 4; Model B1), whereas in Model B2 it was the other way around. (Fig. 4; Model B2). Both models showed the development of dextral strike-slip (antithetic, with respect to sinistral simple shearing) faults along the vertical boundaries of the central domain (Fig. 4a, f). At later stages in the model evolution, the model A2 (composed only by microbeads grains) contains more faults than the model A1 (Fig. 3d and i). The model A1 (only quartz sand) is the only one that develops antithetic (dextral) faults. The final cumulative strain panels for Slightly later, sinistral strike-slip faults (synthetic) formed in the western and eastern domains (4b, g). Although these faults propagated laterally with time, none of the synthetic faults crossed the central domain. Instead, they halted at or close to the boundary faults along the central domain (Fig. 4c, h). In Model B1 a few antithetic faults formed in between pre-existing synthetic faults in the outer domains, striking at c. N60°E (Fig. 4d, e). Antithetic faults developed also in the western and eastern domains of Model B2, almost coevally with the synthetic faults. They strike at higher angles to the shear direction than those antithetic faults confined between overlapping synthetic faults in Model B2. With increasing deformation, the central domain and its bordering antithetic faults rotated counterclockwise in both models (Fig. 4a-e, f-j), as did the antithetic faults in the western and eastern domains, which acquired a slight sigmoidal "S-shaped" form (e.g. Fig. 3e and j) show that most deformation is taken up by a central strike-slip fault that crosses the entire length of the model.

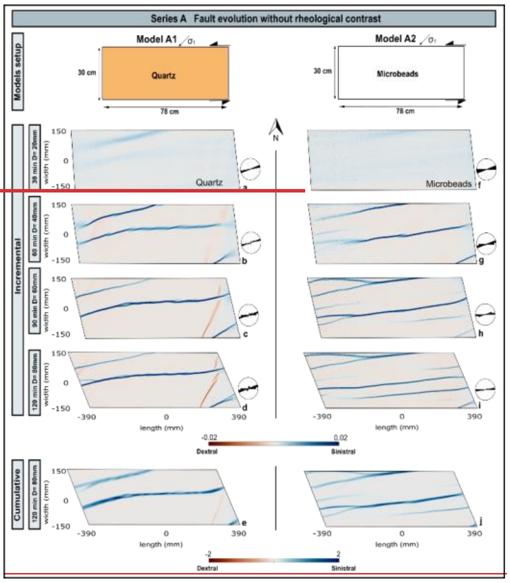
Series A Fault evolution without rheological contrast
Models setup
Model A1
σ1
30 cm
Quartz
78 cm
Model A2
σ1
30 cm
Microbeads
78 cm
Incremental
30 min D= 20mm
60 min D= 40mm
90 min D= 60mm
120 min D= 80mm
width (mm)
150
0
-150
Quartz
Microbeads
N
a
b
c
d
f
g
h
i
-390
0
390
length (mm)
-0.02
0.02
Dextral
Sinistral
Cumulative
120 min D= 80mm
e
j
-2
2
Dextral
Sinistral

4j)

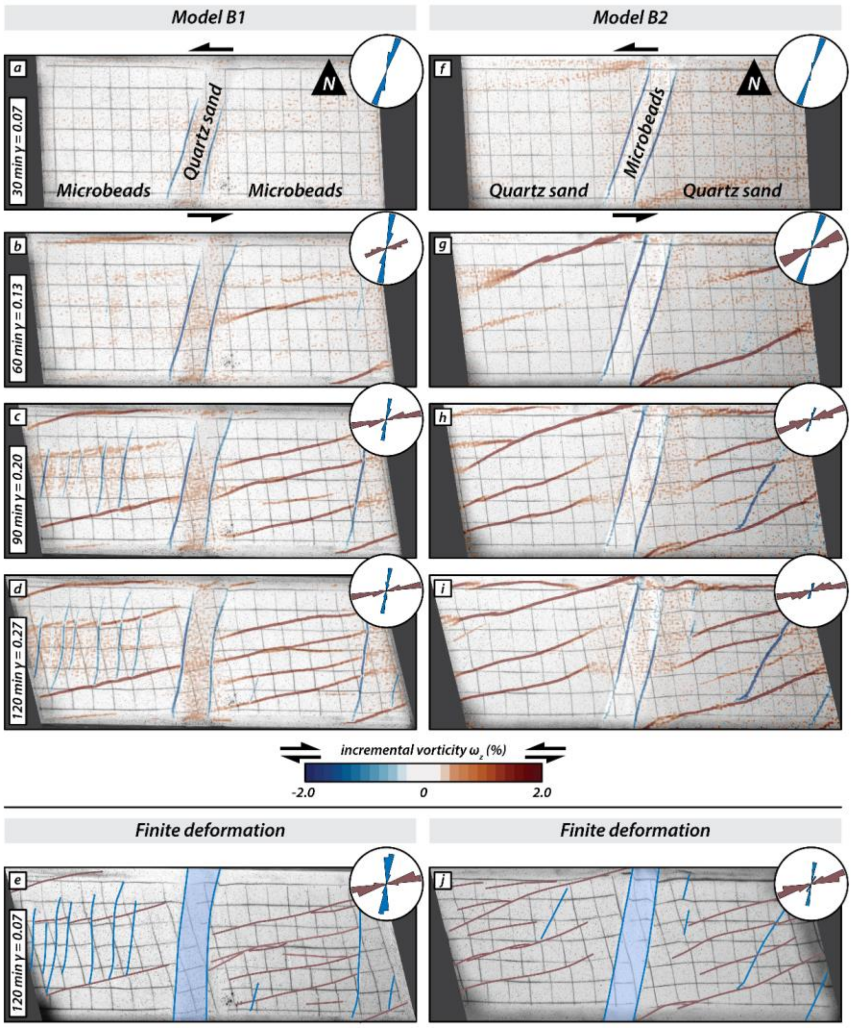

Figure 34: Overview of Series AB models: simpleSimple shear experimentsdeformation of two models with microbeads (Model A1vertical domains of contrasting brittle strength oriented N20°E. The first four panels of each series show surface photographs with the incremental vorticty after 30 minutes (20 mm displacement of mobile base plate), 60 minutes (or 40 mm displacement), 90 minutes (or 60 mm displacement) and quartz sand (Model A2).120 minutes (or 80 mm displacement). Incremental and cumulative positive/ and negative values indicates dextral and indicate sinistral kinematics(synthetic, red) and dextral (antithetic, blue) relative movement, respectively. The last panel for each series shows a surface photograph of the final stage overlain with the interpreted fault pattern; red lines are sinistral faults, blue lines are dextral faults.

~~3.2.~~3.3. Series ~~B.~~C: Fault evolution in models with N-S ~~rheological contrast~~vertical domain boundaries

The Series C models had vertical N-S striking domain boundaries. Model C1 had a 5-cm wide central domain of quartz sand with microbeads on either side (Fig. 5; Model C1), whereas in Model C2 it was the other way around (Fig. 5; Model C2). During the early stages of simple shear, dextral (antithetic) faults formed along the N-S striking borders of the central domain (Fig. 5b, g) in both models, but earlier and more pronounced in Model C1. With progressive shearing, both synthetic and antithetic faults formed in the outer domains of both models (Fig. 5c and h). In Model C2, activity along the antithetic faults bordering the central domain ceased, and synthetic faults propagated from the outer domains into the central weak domain (Fig. 5h-j). In contrast, in Model C1, the antithetic faults along the borders of the central domain remained active, and no synthetic faults crossed the central strong domain (Fig. 5d). In the eastern domain of Model C2, a few antithetic faults formed in between major synthetic faults, striking at a lower angle to the shear direction than earlier formed antithetic faults in the western domain. With progressive simple shear the central domain showed counterclockwise rotation about a vertical axis in both models and antithetic faults obtained a sigmoidal shape as seen in top view (Fig. 5i). As the initial N-S antithetic faults bordering the central domain rotated counterclockwise, activity along these faults diminished and new fault segments appeared striking nearly parallel to earlier formed antithetic faults in the western and eastern domain (Fig. 5d, e). At the final stage of Model C2, antithetic faults dominated in the western domain and synthetic faults in the eastern domain. In contrast, in Model C1, both antithetic and synthetic faults were present in both the western and eastern domain.

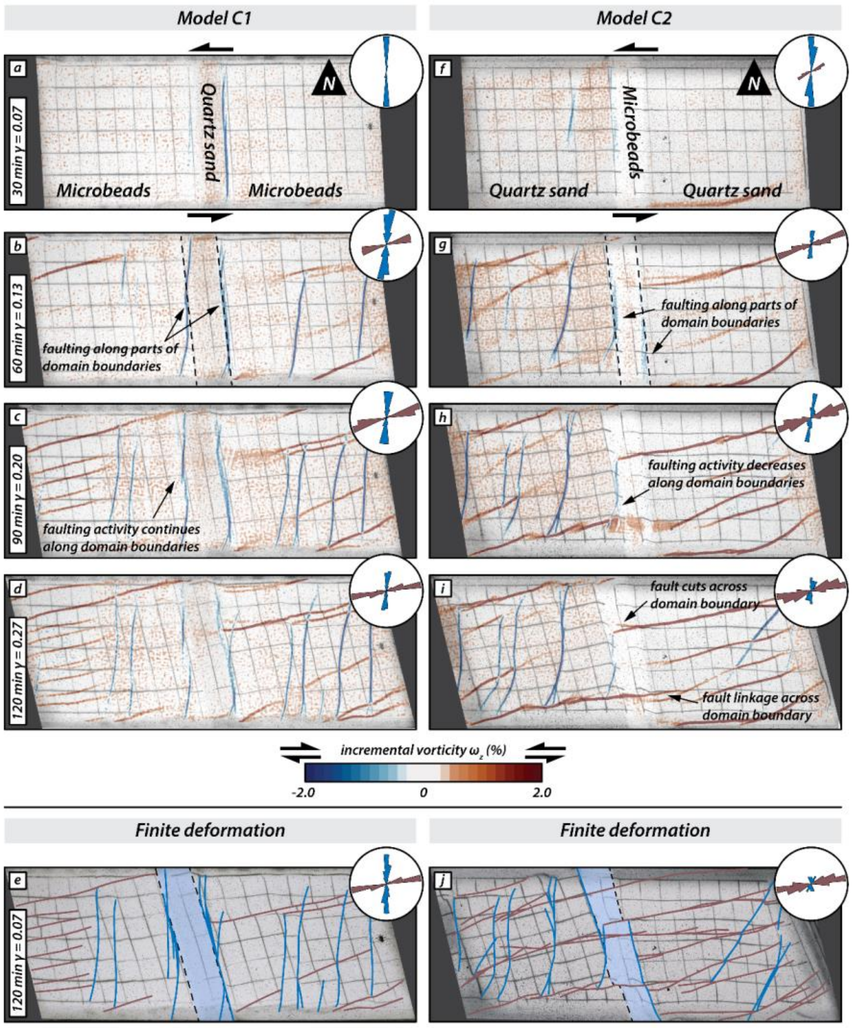

Figure 5: Overview of Series C models: Simple shear deformation of two models with vertical domains of contrasting brittle strength striking N-S. The first four panels of each series show surface photographs with the incremental vorticty after 30 minutes (equivalent to 20 mm displacement of the mobile base plate), 60 minutes (or 40 mm displacement), 90 minutes (or 60 mm displacement) and 120 minutes (or 80 mm displacement). Incremental positive and negative values indicate sinistral (synthetic, red) and dextral (antithetic, blue) relative movement, respectively. The last panel for each series shows a surface photograph of the final stage overlain by the interpreted fault pattern; red lines are sinistral faults, blue lines are dextral faults.

Con formato: Sin Oculto

Con formato: Normal, Sin viñetas ni numeración

Series D The Series B models have rheological contrasts oriented N-S. Model B1 has a 5-cm wide central contrast of microbeads with quartz sand on either side, whereas in Model B2 it is the other way around (Fig. 4). The contrast divides the model in a western and eastern domain, with the central contrast rotating counterclockwise due to the applied sinistral bulk shear.

3.4. In both models, initial simple shear results in reactivation of the N-S rheological boundaries. These are reactivated, showing dextral strike-slip movement (Fig. **: Fault evolution in models with N20°W striking vertical domain boundaries**

In the series D models the orientation of the vertical central domain was N20˚W. In Model D1 the central domain consisted of a 5 cm-wide central band of quartz sand with microbeads on either side (Fig. 6; Model D1), whereas in Model D2 it was the other way around (Fig. 6; Model D2). In contrast to the Model C series, no faults formed along the boundaries of the central domain in both Models D1 and D2 (Fig. 6a and f). Model D1 is dominated by synthetic faults crosscutting the central strong domain (6c-e). As these faults traversed the central domain, they slightly changed their strike orientation. In contrast, in Model D2 the weak microbeads of the central domain were internally deformed and oblique-slip reverse faults formed, which propagated laterally and parallel to the domain boundaries (Fig. 6g-j). Synthetic faults formed both in the western and eastern domain of Model D24a, f). The antithetical faults are the first ones generated, firstly in model B1. As in the previous series, the models with microbeads grains take longer to localize the deformation. With increasing shearing, deformation tends to be compartmentalized and two domains are distinguished in both models. In Model B1, sinistral, synthetic faults form in the eastern domain whereas both sinistral and dextral faults form in the western domain (Fig, 4c). In contrast, in Model B2, it is the other way around, the eastern domain contains both sinistral and dextral faults, whereas the western domain shows sinistral faulting (Fig. 4h). In both models, the antithetic, dextral strike-slip faults in the western (Model B1) and eastern domains (Model B2) are striking at different angles than those along the vertical contacts of the central contrast. Whereas the reactivated dextral faults along the vertical N-S contacts initially strike N-S, the newly formed dextral faults in the adjacent domains strike N20°E. Model B1 and N7-10°E in Model B2. Because of the bulk sinistral simple shear, the central band and the dextral faults at both contacts rotate counterclockwise, and as they propagate, they acquire a slight S-shape in surface view (Fig. 4b, g). Sinistral faults developed in Model B1 propagate along strike crosscutting the central weak band composed of microbeads, striking W-E in the central domain which differs from the initial strike (Fig. 4c, d). At the same time, the dextral reactivation along the vertical contacts diminishes. However, in Model B2 no sinistral faults cut the central strong contrast composed of quartz sand. This model shows is a greater number of sinistral faults than Model B1. These faults are located in the microbeads, maintain the same spacing between them (fig. 4h and i).

The cumulative strain panels show for both models that most of the deformation is accommodated by sinistral faults, with dextral fault activity restricted to the western domain in Model B1 and to the eastern domain in Model B2 (Fig. 4e, j).

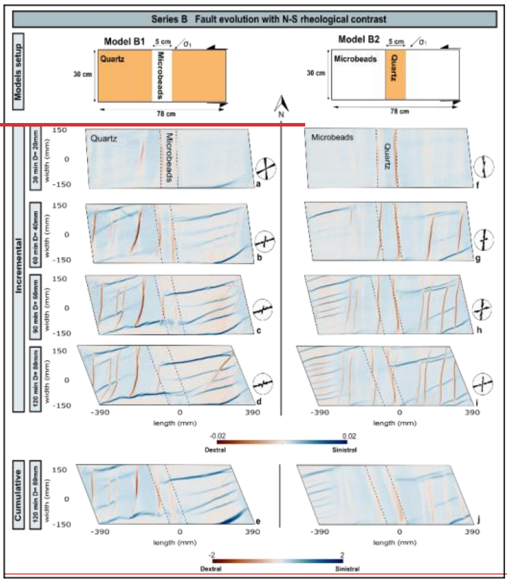

Figure 4: Overview of Series B models: simple shear experiments with a vertical N-S oriented rheological contrast consisting of a 5 cm wide band of microbeads (Model B1) or quartz sand (Model B2) in the central part of the model. Incremental and cumulative positive/negative values indicates dextral and sinistral kinematics, respectively.

3.3. Series C. Fault evolution with N20°W rheological contrast

In the series C models the vertical rheological contrasts oriented N20˚W, with a 5 cm-wide central band of microbeads and quartz sand on either side, in Model C1 and vice versa in Model C2 (Fig. 5). In contrast to the Model B series, no reactivation of the rheological contacts occurs in these series. After 1 hour, two synthetic sinistral faults are generated in Model C1 (Fig. 5b) at the corners of the model, while Model C2 only develop one sinistral fault in the eastern corner (Fig. 5g). The strike of the synthetic faults varies between the two models, N76˚E in Model C1 (Fig. 5c) and N80˚E in Model C2. The same occurs with the

~~antithetic faults developed at the end of the models. The antithetic faults strike N27˚E in Model C1 (Fig. 5c, d) and N9˚E in Model C2.~~

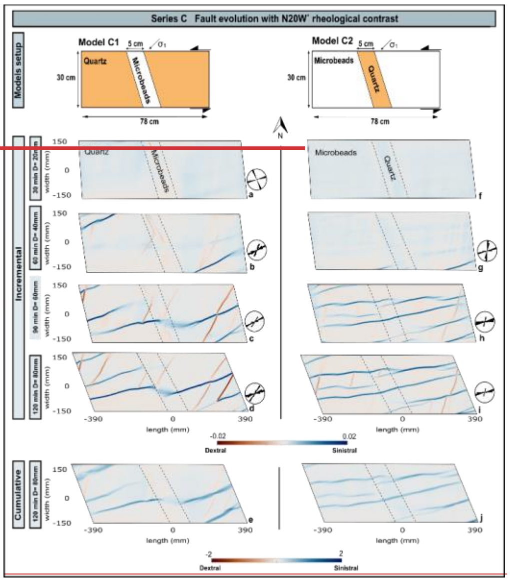

, while antithetic faults formed later and in between overlapping synthetic faults (Fig. 6g-j). With progressive deformation synthetic faults from the western and eastern domain in Model D2 propagated partially into the central, weak domain, but halted at the previously formed oblique-slip reverse faults (Fig. 6h and i). During late stages of deformation a few antithetic faults formed in Model D1 in between earlier formed synthetic faults, striking at somewhat larger angles to the shear direction than in Model D2.

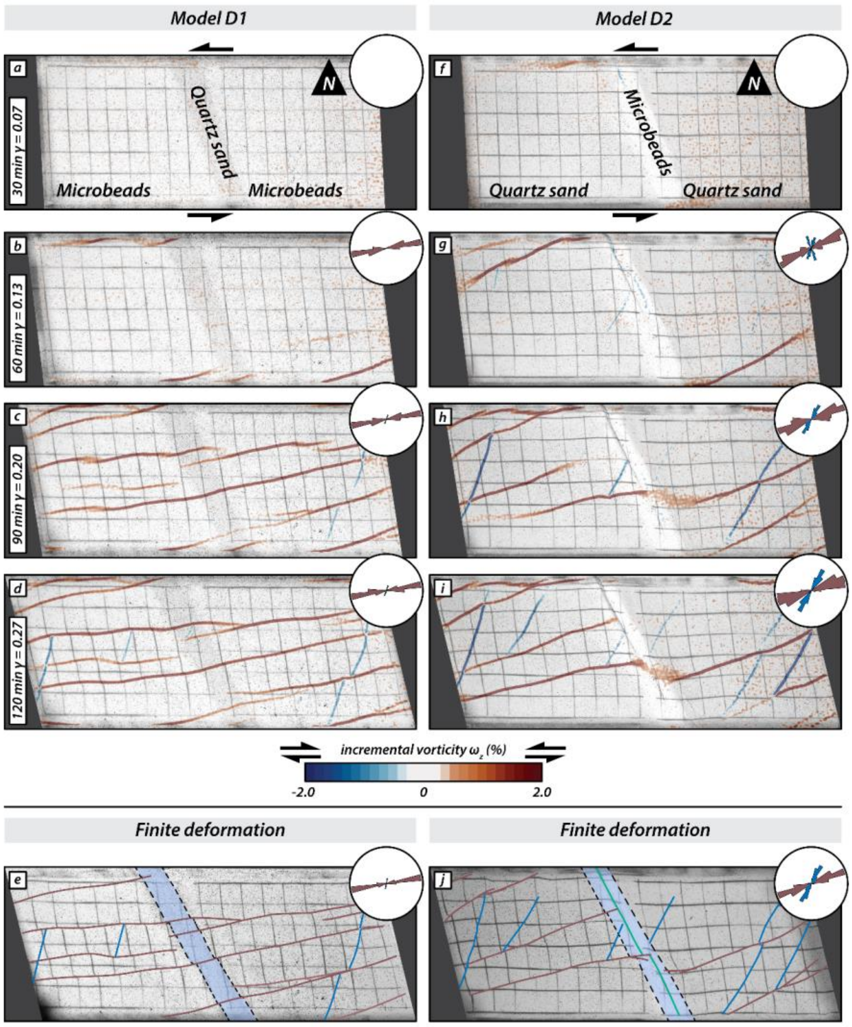

Figure 56: Overview of Series C models: simple shear experimentsD models: Simple shear deformation of two models with N20°W striking vertical domains of contrasting brittle strength. The first four panels of each series show surface photographs with a vertical N20° W rheological contrast consisting the incremental vorticty after 30 minutes (20 mm displacement of a 5 cm wide band of microbeads (Model C1) mobile base plate), 60 minutes (or quartz sand (Model C2) in the central part of the model.40 mm displacement), 90 minutes (or 60 mm displacement) and 120 minutes (or 80 mm displacement). Incremental and cumulative positive/ and negative values indicate sinistral (synthetic, red) and dextral and sinistral kinematics(antithetic, blue) relative movement, respectively.

In these models' series, the introduction of the central contrast does not affect the behavior of both models and there are no domains. There are more sinistral faults in model C2 than in model C1 (Fig. 5c and h), and both cut the central band. In Model C1, when these faults reach the contact The last panel for each series shows a surface photograph of the final stage overlain with the microbeads, they change their strike turning clockwise, resulting in an overall E-W releasing band (Fig. 5c, d). At the same time, deformation in the central band is less localized. Unlike Model C1, the synthetic interpreted fault pattern; red lines are sinistral faults in Model C2 change its strike counterclockwise when they cut the central contrast (Fig. , blue lines are 5i).

The cumulative strain panels clearly show that most deformation in both models is taken up by synthetic, sinistral faults. Model C1 shows little deformation in the central domain with synthetic faults abutting at the rheological contrast on either side, with diffuse deformation within the central band. In contrast, Model C2 shows synthetic faults throughout the model cutting across the central domain of quartz sand with deformation being less diffuse in the central domain.

3.2.

3.3.

3.4. Series D. Fault evolution with N20°E rheological contrast

The vertical rheological contacts in the Series D models oriented N20°E, with a 5-cm wide central contrast composed by microbeads surrounded by quartz sand in Model D1 and vice versa in Model D2 (Fig. 6). As in the models' series B, the rheological boundaries are reactivated with **dextral** strike-slip movement (Fig. 6a and f) and three fault domains are generated. With increasing shearing, model D1 develops 5 sinistral faults (Fig. 6 b). In contrast, model D2 only develop one clear sinistral fault and the antithetic faults begin to show slightly in the model (Fig. 6g). As in the previous models, the strike of these synthetic faults varies. The synthetic faults in the quartz sand strike N77˚E, whereas in the microbeads is N80˚E. In Model D2, the antithetic faults strike N7˚E become more prominent, particularly in the western domain. They accommodate more displacement and rotate at the same time counterclockwise with almost N-S orientation (Fig 6h, i). Unlike Model D2, Model D1 barely registers antithetic faults, and their strike is N17˚E. Although the model with predominantly microbeads(D2) takes longer to localized the deformation, it registers a greater number of faults at the end than the model with predominantly quartz sand (D1).faults,

In both models, localized deformation is not transferred through the central band and the sinistral faults do not connect (Fig. 6c and h). With increasing shear, despite the predominance of dextral faults in model D2, the cumulative strain panels (Fig. 6e, j) clearly show the dominance of sinistral strike-slip faulting in the western and eastern domains for both models.

Con formato: Fuente: 9 pto, Negrita
Con formato: Fuente: 9 pto, Negrita
Con formato: Sin Oculto
Con formato: Normal, Sin viñetas ni numeración
Con formato: Interlineado: Múltiple 1,15 lín.
Con formato: Fuente: 9 pto, Negrita
Con formato: Fuente: 9 pto, Negrita

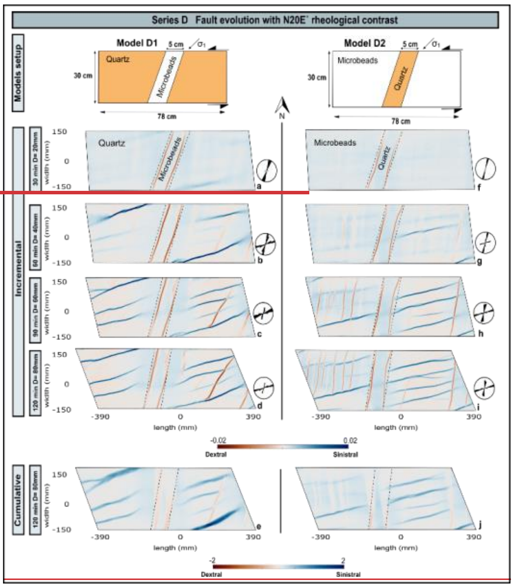

Figure 6: Overview of Series D models: simple shear experiments with a vertical N20° lithology contrast band 5 cm, composed of microbeads grains (Model D1) and quartz sand (Model D2). Incremental and cumulative positive/negative values indicate dextral and sinistral kinematics. respectively.

4. Discussion

We used granular materials with contrasting rheologies performed analogue modelling experiments to test the influence of vertical contrasts, upper crustal domains of contrasting strength on the development and evolution of strike-slip fault zones. It must be noted that the vertical lithological boundaries are reactivated during model construction when the thin cardboard sheets, used to separate the two granular materials, are removed.

We first discuss the results of our models without any vertical rheological contrast (4.1). Then, we are going to discuss the obtained results from the addition a vertical contrast in the model (4.2) Finally, we compare our results with a natural example (4.3).

Con formato: Fuente: Negrita, Oculto

Con formato: Esquema numerado + Nivel: 1 + Estilo de numeración: 1, 2, 3, … + Iniciar en: 1 + Alineación: Izquierda + Alineación: 0,63 cm + Sangría: 1,27 cm

4.1. Models without vertical rheological contrast

In our models without a vertical rheological contrast (Models A1 and A2), the deformation is accommodated by synthetic, sinistral strike-slip faults (Fig. 7a and i). The deformation takes more time to be localized in models containing the weak material (model composed only by microbeads grains; Model A2; Fig. 7i and m) than in models composed by the strong material (model composed only by quartz sand; Model A1; Fig. 7a and e). However, the experiment composed by this weaker and rounded material shows the highest number of faults at the end of the experiment (Model A2) (Fig. 7i). This phenomenon could be due to the size and shape of the materials. The more equal are the grain size and shape, like microbeads grains, the less deformation concentrate (Antonellini et al., 1994., Mair et al., 2002). This deformation pattern was also observed by Aydin and Berryman, 2010; Li et al., 2021; Cheng et al., 2022 and Venancio and Alves Da Silva, 2023.

The strike of the faults in the models with the strong material is N72°E (Fig. 7e). On the contrary, the initial strike of the faults in models with weaker material is N81°E (Fig. 7m). As the granular materials have a coefficient of internal friction of 36° for quartz sand and 22° for microbeads (Anderson, 1951; Panien et al., 2006; Dooley & Schreurs, 2012) they have a different rupture criteria (Mohr-Coulomb).

4.2. Models with a vertical rheological contrast

When a horizontal rheological contrast is imposed, a series of changes in the stress field are induced, resulting in different fault kinematics and fault propagation patterns (Segall and Pollard, 1983; Peacock, 1991; Peacock and Sanderson, 1992; Livio et a., 2020). In addition, the heterogeneity of the models is determinant for the structure and chronology of the faults (Viola et al., 2004; Schellart and Strak, 2016; Lefevre et al., 2020; Venancio and Alves Da Silva, 2023).

As in the article from Gomes et al (2019), in our models, the addition of a *vertical* rheological contrast results also in different fault patterns comparing with models without a vertical contrast. Moreover, the fault patterns became more complex considering the of two reference models which simulated a uniform upper, brittle crust (section 4.1). Subsequently, we discuss and compare the results of three series of models (Series B, C and D, in which two different brittle materials, strong quartz sand and weak microbeads,

Con formato: Inglés (Reino Unido)

alternated to form three vertical domains of contrasting strength (section 4.2), i.e. either weak-strong-weak (i.e. quartz sand-microbeads-quartz sand) or strong-weak-strong (i.e. microbeads-quartz sand-microbead section). Each of these three series had a different orientation of the vertical contact. The introduction of a vertical contrast oriented N-S and N20˚E, influences on: (1) the number of faults is greater if the contrasts are N-S oriented (Fig. 7c and k); (2) greater number of antithetic faults. (Fig. 7o and p). These setups create two domains with rectangular shapes (shorter on the X axis and longer on the Y axis), inducing the model to be compartmentalized. This geometry will change the final fault pattern and promotes the development of antithetic, dextral faults (Garfunkel and Ron, 1985; Capais et al., 1991; Dooley and Schreurs, 2012).

Con formato: Inglés (Reino Unido)

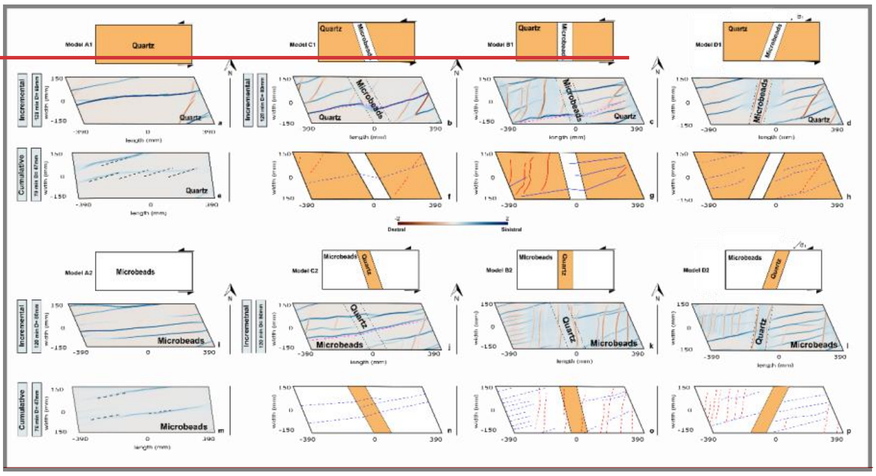

Figure 7: Overview of the main stages of the experiment with schematic drawings depicting the final result.

The initial strike of the antithetic, dextral faults is N10˚E in zones composed by the weak material and N7˚E in the strong materials. However, as the models progress the final fault strike for both types of models became more N-S and showing a S-shape for the models with the weak material in the center (Fig. 7o and p). This phenomenon could be related to block rotation (Garfunkel and Ron, 1985; Deng et al., 1986), which is a process that occurs in nature (Ron et al., 1984, domains with respect to the shear direction. In section 4.3 we discuss how1986; Nicholson et al., 1986; Sylvester, 1988; Sorlien et al., 1999; Dooley and Schreurs, 2012; Kavyani-Sadr et al., 2022). The initial strike of the synthetic, sinistral faults remains the same during the whole experiment, being N70°E for models predominating the strong material and N80°E for models with the weak one (Fig. 7b and j).

If the central vertical domain affects fault interaction and/or fault linkage. In the final section 4.4 we compare modelling results with a strike-slip fault system in the Iberian Peninsula.

Con formato: Inglés (Reino Unido)

4.1. Series A: Strike-slip faulting in models with a homogeneous upper brittle layer

Initial bulk simple shear is accommodated in both models by zones of diffuse deformation and is followed by localized deformation along narrow fault zones. It is interesting to note that localization requires a higher shear deformation in the model with the weak microbeads than in the model with quartz sand. This difference in localization behaviour is attributed to the difference in dilatancy between the two analogue materials, which is closely related to grain shape and grain size distribution. The microbeads are well-rounded and have a narrow grain size distribution (150-210 µm), whereas the quartz sand grains are angular and have a wider grain size distribution (60-250 µm). The more equal the grain shape and grain size, the more applied shear deformation is needed before strain localizes along a narrow fault zone (Antonellini et al., 1995; Mair et al., 2002).

Sinistral (synthetic) strike-slip faults form in both models. The initial strike of these faults differs between the model with microbeads and the one with quartz sand, striking at c. N79°E and N72°E, respectively. The synthetic fault orientations reflect the Mohr-Coulomb fracture criterion for faulting in a homogeneous material (Fig. 7). At the onset of simple shear, the main principal stress, σ_1 is oriented at 45° to the shear direction, and the two potential fault orientations strike at 45° - ϕ/2 and at 45° + ϕ /2 to σ_1, respectively with ϕ the angle of internal peak friction i.e. the synthetic and antithetic faults would strike at N79°E and N11°E, respectively in the model with microbeads and at N72°E and N18°E, respectively in the model with quartz sand. In our models only the synthetic faults form during the early stages of simple shear deformation. The early synthetic faults form a right-stepping *en echelon* fault pattern that link up with increasing deformation to form major strike-slip faults. The fact that nearly all deformation is taken up by synthetic faults is typical of simple shear models with an initial rectangular shape, i.e. a large aspect ratio of length (parallel to shear direction) divided by width (Schreurs, 2003; Dooley & Schreurs, 2012). A comparison of previous simple shear experiments shows that the shape of the initial model has a clear influence on the relative proportion of synthetic and antithetic faults (Gapais et al., 1991; Schreurs, 2003). With decreasing aspect ratio, the number of antithetic faults will increase, and in case of an initially square-shaped model, (i.e., aspect ratio is 1) antithetic faults will dominate (Gapais et all., 1991; Dooley &

Schreurs, 2012). In the model with quartz sand, a few antithetic faults form in between previously formed major synthetic faults (Fig. 3i). These late antithetic faults, however, form in response to local stress field modifications between overlapping synthetic faults, causing σ_1 to rotate clockwise from 45° to the bulk shear direction towards an orientation that is subparallel to the previously formed synthetic faults. As a consequence, these late antithetic faults are not in the "conjugate" position with respect to the synthetic major faults, but strike at lower angles with respect to the long borders of the model (these are the lower-angle antithetic faults of Schreurs, 2003).

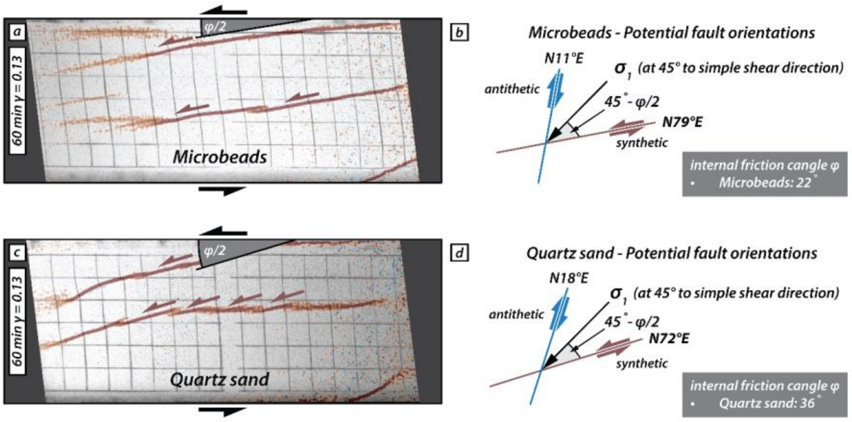

Figure 7: Illustrative scheme of the expected fault orientation according to the Mohr-Coulomb failure criteria, for the experiments with only one type of material (homogeneous upper crust). a) and c) Surface photographs of the model with microbeads only (a) and quartz sand only (c), with the incremental vorticty after 60 minutes (40 mm displacement). b) and d) Schematic explanation for the expected orientation of the synthetic and antithetic faults considering the simple shear orientation along with the Mohr-Coulomb failure criteria, for the models with microbeads and quartz sand only respectively.

4.2. Series B, C and D: The influence of the orientation of vertical domains of contrasting brittle strength on strike-slip faulting

Introducing vertical domains of contrasting brittle strength in our models results in fault patterns that differ when compared to the Series A models that consisted only of one homogeneous brittle material. The degree of difference in the fault pattern is a function of the orientation of the vertical domains and whether the domains have a strong (quartz sand) or weak (microbeads) material in the central domain. Fig. 8 shows a schematic overview of the final structures of all six models which had vertical domains of contrasting brittle strength. Each of these six models had an initial rectangular shape and consisted of a western, central and eastern domain with the central one having a contrasting brittle strength with respect to the adjacent, outer domains. The initial strike of the vertical domain boundaries, either N20°E, N-S or N20°W has a profound influence on the resulting fault pattern.

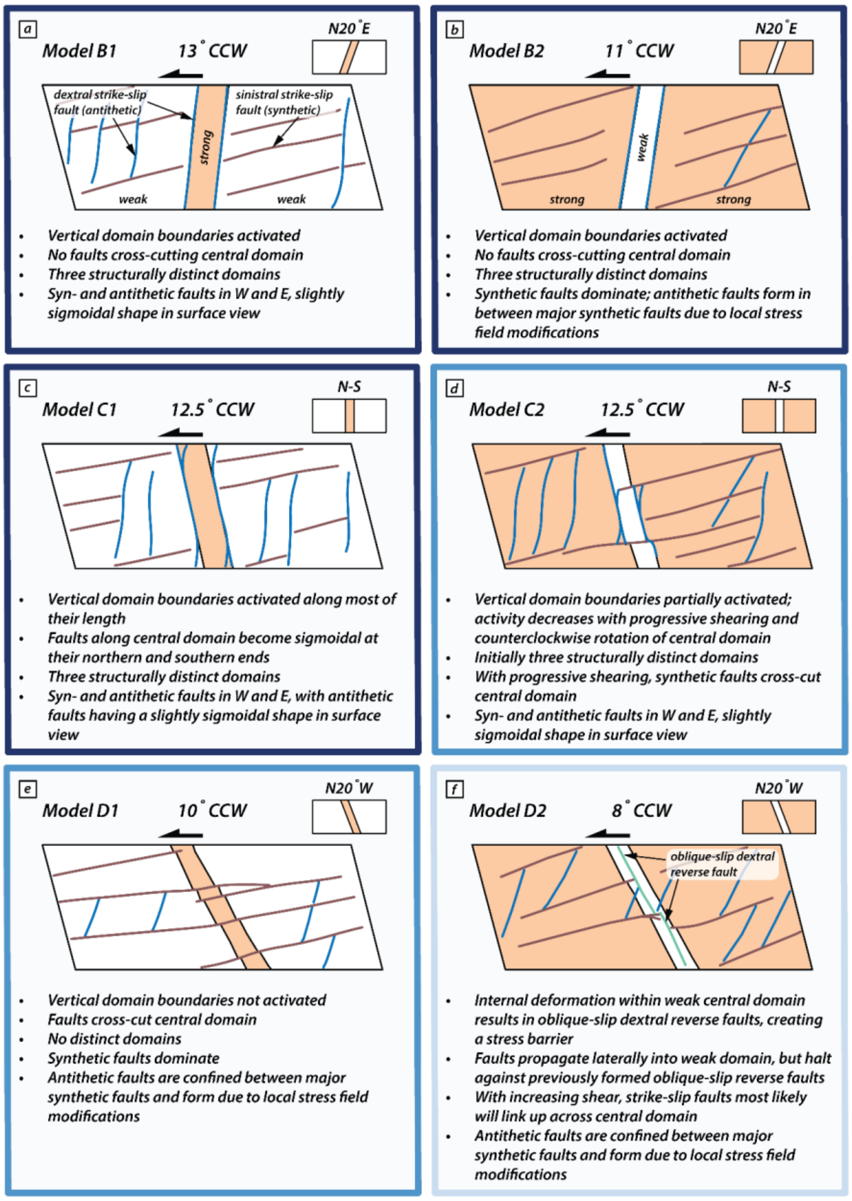

Figure 8: Schematic surface views summarizing the main results from the models with vertical domains of contrasting brittle strength.

The domain boundaries in Series B models initially strike N20°E, which is close to the antithetic fault orientation predicted by the Mohr-Coulomb failure criterion (i.e. N11°E for microbeads and N18°E for quartz sand, see section 4.1). As a result the domain boundaries in both models are activated along their entire length, forming antithetic, dextral strike-slip faults along them (Fig. 8a,d). With progressive sinistral simple shear, the central fault-bounded domain rotates counterclockwise about a vertical axis, and at the end of the experiment has rotated by about 12° striking c. N08°E. The domain boundaries remain active throughout the model run, because their strike orientation remains close to the antithetic fault orientation predicted by the Mohr-Coulomb failure criterion (Fig 8a, b). As a result of continuous fault activity along the central domain boundaries, each of the two Series D models develops three spatially separated structural domains: a western and eastern domain, containing both synthetic and antithetic faults, separated from a central domain bordered by antithetic faults. Faulting is thus compartmentalized within the model and no faults propagate from the outer domains into the central domain (Fig. 8a, b).

In comparison to the Series B models, the initial N-S strike of the central domain boundaries in the Series C models (Fig 8c, d) is less favorably oriented with respect to the antithetic fault orientations predicted by the Mohr-Coulomb failure criterion. As a result, the domain boundaries in both models are only partially activated dextrally during initial simple shear deformation (Fig. 4). During progressive shearing the domain boundaries rotate counterclockwise and become even less favorably oriented for further activation and fault branches partially no longer follow the domain boundaries, with the overall fault geometry at and in the vicinity of the central domain boundaries acquiring an overall "S-shaped" geometry in surface view (Fig. 8c, d). The difference between Model C1 (weak-strong-weak) and Model C2 (strong-weak-strong) is that in the former the total length of the domain boundaries activated is larger and faults at or in the immediate vicinity of the domain boundaries remain longer active than in the latter (compare Fig. 8c and d). This difference can be explained by the fact that in Model C1 the weak microbeads represent the dominant brittle material, and the antithetic fault orientation predicted by Mohr-Coulomb, N10°E for a homogeneous microbeads layer, is close to the initial N-S orientation of the domain boundary. In contrast, Model C2 is dominated by quartz sand and the antithetic fault orientation predicted by Mohr-Coulomb, N18°E for a homogeneous quartz sand layer, is farther away from the initial N-S striking central domain and consequently domain boundaries are less activated and fault activity decreases more rapidly with progressive deformation. As a consequence in Model C2, synthetic faults forming in the outer domains can propagate across the poorly activated domain boundaries, cross-cutting the central domain, and can partly link up to form major through-going faults. In Model C1, however, fault activity along domain boundaries was stronger and occurred longer, and the domain boundaries form a more effective barrier and no synthetic faults cross-cut the central domain.

In comparison with the Series B and Series C models, the initial N20°W striking central domain boundaries in the Series D models are the least favorably oriented for fault activation. In the weak-strong-weak Model D1 (Fig. 8 e and f), the domain boundaries are not activated at all and the synthetic faults forming in the outer domains propagate across the central domain. Apart from a slight re-orientation of the fault strike, reflecting the difference in material strength between central and outer domains (difference in internal friction angles), the fault pattern in Model D1 is very similar to the one in Model A1, which had no vertical brittle strength contrasts. The strong-weak-strong Model D2 shows a different deformation behaviour. Although the domain boundaries at the surface are not activated, the presence of a weak material surrounded by strong material results in internal deformation within the central domain and dextral oblique-slip reverse faults form striking parallel to the domain boundaries. These faults prevent synthetic faults from crossing the central domain, and they halt against the oblique-slip reverse faults.

In all models with vertical domains of contrasting brittle strength, the orientation of the sinistral, synthetic faults forming in the outer domains reflects the Mohr-Coulomb failure criterion, i.e. if the outer domains consist of weak microbeads, with an internal friction angle of 22°, the strike of the synthetic faults is c. N79°E and when the outer domains consist of strong quartz sand, with an internal friction angle of 36°, the strike of the synthetic faults is c. N72°E (see also section 4.1). In those models, in which the synthetic faults cross-cut the central domain, the strike of the faults changes slightly, due to the difference in internal friction angles between the quartz sand and the microbeads (Du and Aydin, 1995; de Doney et al., 2011).

The antithetic faults that form in the outer domains of our models are of two types: (i) those that form relatively early in as yet largely unfaulted domains and strike at large angles to the shear direction and (ii) those confined between earlier formed and overlapping synthetic faults that strike at lower angles to the shear direction. The early-formed dextral, antithetic faults reflect the orientation predicted by the Mohr-Coulomb failure criterion, striking c. N18°E if the outer domains consist of quartz sand and c. N11°E if the outer domains consist of microbeads. Due to lateral fault propagation and coeval rotation of the central fault segments, these antithetic faults obtain a slightly S-shaped sigmoidal form in map view during progressive simple shear (see also Schreurs, 1994, 2003; Dooley and Schreurs, 2012). The antithetic faults that are confined in between closely spaced, earlier formed, synthetic faults have an initial different strike (c. N15°-N20°E in microbeads domains, e.g. Model C1) and c. N25°-N30°E in quartz sand domains, (e.g. Model C2), which is clearly different from those antithetic faults formed during early stages in largely unfaulted domains. The antithetic faults confined between major synthetic faults result from local stress field modifications governed by relative movement of material in between previously formed synthetic faults with large overlap (Schreurs, 2003; Dooley and Schreurs, 2012; their R'_L faults). Both types of antithetic faults rotate counterclockwise with progressive sinistral simple shear. Rotation of faults and blocks in strike-slip fault systems is not only observed in analogue models (Schreurs, 1994, 2003; Dooley and Schreurs, 2012), but has also been documented in nature (e.g., Ron et al., 1986; Nicholson et al., 1986contrast is oriented N20°E, the faults do not cut the contacts (even when the material is the weaker one; Fig. 7h and p). When the contrast is oriented N-S and is composed of the strong material, the faults do not cut the rheological contrast (Fig. 7k and o). However, if the weaker material constitutes the rheological contrast, the sinistral faults crosscut the contact changing their strike from N70°E to E-W (Fig. 7c and g). The only series models that show faults cutting the contrast, despite the properties of the material, are the models with the oriented contrasts N20˚W (models C1 and C2; Fig. 7b, f, j and n). If the contrast is constituted of a weaker material, the initial fault strike turns clockwise to a more like E-W as in model B1 (Fig. 7f). On the contrary, the faults that crosscut the strong material turns counterclockwise striking approximately N45˚E (Fig. 7n). This change in the strike of the faults could be related to the internal friction angle of the unit cut (Du and Ayin). It is thus important to keep in mind that antithetic faults (and blocks in between) can undergo considerable rotation about a vertical axis during simple shear deformation, implying that present-day antithetic fault orientations in strike-slip fault systems do not necessarily reflect the orientations in which they initially formed.

4.3. Fault linkage across central domain

In models where synthetic faults from the eastern and western domain cross-cut the central domain, the entire model behaves as one domain. As shown in the section above, this is the case for models C2, D1, and D2 where the vertical boundaries of the central domain are not or only partially activated, depending on the orientation of the central domain (section 4.2). However, all three models show distinct differences in how laterally propagating synthetic strike-slip faults link across the central domain (Fig. 9). For model D1 (Fig. 9a, b), faults cross-cut the stronger (i.e., quartz sand) central domain from the E and W domains (Fig. 9a) and eventually link in the E domain (Fig. 9b). Across the central domain, the fault strike changes according to the predicted Mohr-Coulomb failure criterion resulting in a step-like linkage pattern in surface view (i.e., flat-steep-flat; Fig. 9a, b).

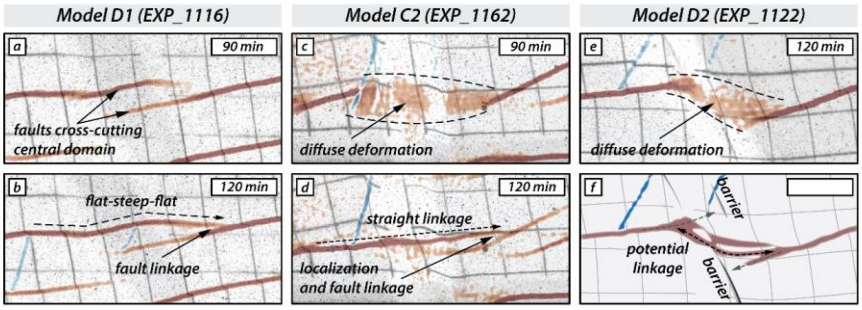

Figure 9: Surface detailed photographs of the central domain of the models with the contrasting brittle mechanical strength, showing the fault linkage across the central domain at 90 minutes (60 mm displacement) and 120 minutes (80 mm displacement). a) and b) model D1 with the central domain striking N20˚W and composed by the strong material (quartz). c) and d) model C2 with the central domain striking N-S and composed by the weak material (microbeads). e) model D2 with the central domain striking N20˚W and composed by the weak material (microbeads). f) Schematic drawing for the fault linkage at the last stage.

For models C2 and D2, however, the domain configuration strong-weak-strong has implications for fault linkage. As synthetic strike-slip faults propagate from the western and eastern domains towards the weaker central domain, early deformation patterns are characterized by a zone of diffuse deformation across the central domain (Fig. 9c, e). In model C2, the fault from the W domain cross-cuts the weak central domain and eventually links with the fault in the E domain in a straight fashion after 120 min (Fig. 9d), abandoning earlier active fault strands striking N18°E (i.e., the predicted orientation for Mohr-Coulomb failure criterion). Similar fault kinematics should be expected for model D2 (Fig. 9e, f). However, laterally propagating faults in the western and eastern domain do not link during the duration of the model run. Instead, the two fault segments halt at the domain boundary resulting in ongoing diffuse deformation without strain localization in the central domain. This behavior may be explained by the presence of the

N20°W-striking reverse faults within the central model domain. Due to the misalignment between central domain boundaries and the expected orientation of antithetic faults, the domain boundaries do not activate and domain-internal deformation is taken up by oblique-slip dextral reverse faults. Such faults (i.e., nearly orthogonally striking with respect to synthetic faults) accommodate bulk shear deformation hindering the synthetic faults to propagate. In that sense, the oblique-slip reverse faults act as an impenetrable barrier inhibiting linkage of synthetic faults across the weak central domain (Fig. 9f). Oblique-slip reverse faults in the central domain, therefore, influence fault interaction across the central domain in a similar way as do the activated domain boundaries in models B1, B2, and C1 (Fig. 8).

4.4. Comparison with strike-slip fault zones in Iberia

The NW Iberian Peninsula contains major sinistral and dextral strike-slip intraplate fault systems (Fig. 10a). These groups on intraplate fault systems are located in an old basement developed during Variscan Orogeny (Devonian-Carboniferous, e.g., Matte, 1991; Martínez Catalán et al., 1997; Fernández et al., 2004), during this stage a set of lithologic units with contrasting properties such as granites, quartzites, slates and high-grade metamorphic rocks were emplaced and deformed. During the Alpine Compression (Late Cretaceous to the present), the present fault pattern was obtained due to the collision between the Iberian microplate and the northern edge of Africa in the middle Miocene (e. g., Alonso et al., 1996; Vegas et al., 2004; Martín-González and Heredia, 2011, Martín-González et al., 2012). This collision caused the Iberian Peninsula to undergo a counterclockwise twist, resulting in slight shearing (e.g. Martínez Catalán, 2011; Vergés et al., 2019). In the study area, intraplate deformation led to a fault pattern primarily composed of sinistral faults, such as the Penacova-Régua-Verin (PRVF), Manteigas-Vilariça-Bragança (MVBF), and Orense faults (see Fig. 10a). Additionally, antithetic dextral faults were also generated (see Fig. 10a).

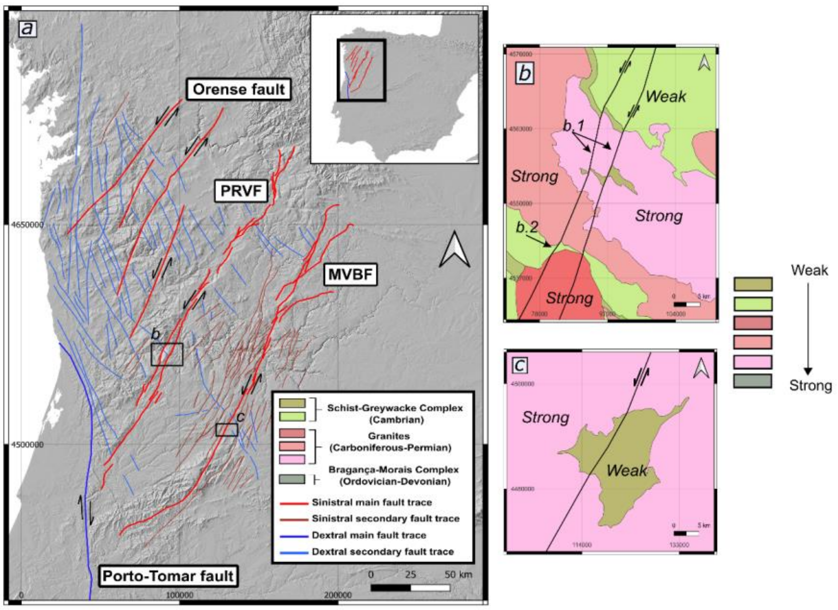

Figure 10: a) Digital elevation model of the northwest section of the Iberian Peninsula where the main faults are drawn, with the location of Figures b and c. The faults are essentially sinistral and there is a dextral fault on the southern edge that delimits the study area. In blue and light red, the secondary antithetic (dextral) and synthetic (sinistral) faults have been marked respectively. b) Schematic representation of the southern section of the Verin fault showing patterns of directional changes similar to models D1 and D2. c) Schematic representation of the southern section of the Vilariça fault showing a similar deformation pattern to model C2.

Among the traces of these faults, we can observe antithetic faults that do not connect with each other and, in some cases, acquire an S shape as described in the C1 and C2 models (Fig. 8). These antithetical faults are not in a conjugate position and are confined between the sinistral faults. At the end of the sinistral faults is the Porto-Tomar fault, which delimits the study area. The Porto-Tomar fault shows dextral displacement and tectonically delimits the area to the north and south of Portugal (Veludo et al., 2017). The main trace of the sinistral faults is not completely straight and undergoes small changes that are observable at a larger scale (Fig. 10b and c). Along the same trace of the PRV fault, it is observed that the faults undergo a counterclockwise refraction, similar to the D1 model with quartz in the central domain (Fig. 10b). On the other hand, in section b.2, the fault undergoes a clockwise refraction as it crosses shale-type materials (which is represented by the microbeads grains in our models; Panien et al., 2006), similar to the D2 experiment. This phenomenon is also observed in the Vilariça fault when the fault intersects granites and slates units (Fig. 10c).

~~, 1995; de Doney et al., 2011).~~

~~4.3. Natural example~~

~~The NW Iberian Peninsula is located in the Iberian Massif (Fig. 8a), a Variscan basement (Paleozoic in age) deformed during two orogeny processes: the Variscan and the Alpine Orogenies (Arthaud and Matte, 1975; Vegas et al., 2004; Martín-González and Heredia, 2011; Martínez Catalán, 2012; Gutiérrez-Alonso et al., 2015; Díez Fernández and Pereira, 2016). The area contains two major intraplate fault systems: the Penacova-Régua-Verin (PRV) and the Manteigas-Vilariça-Bragança (MVB) (Fig. 8b). These NNE-SSW left-lateral strike-slip faults are longer than 200 km and crosscut three main lithologies domains, from stronger to weaker: (1) Bragança-Morais Complex, (2) Granites and (3) Schist-Greywacke Complex.~~

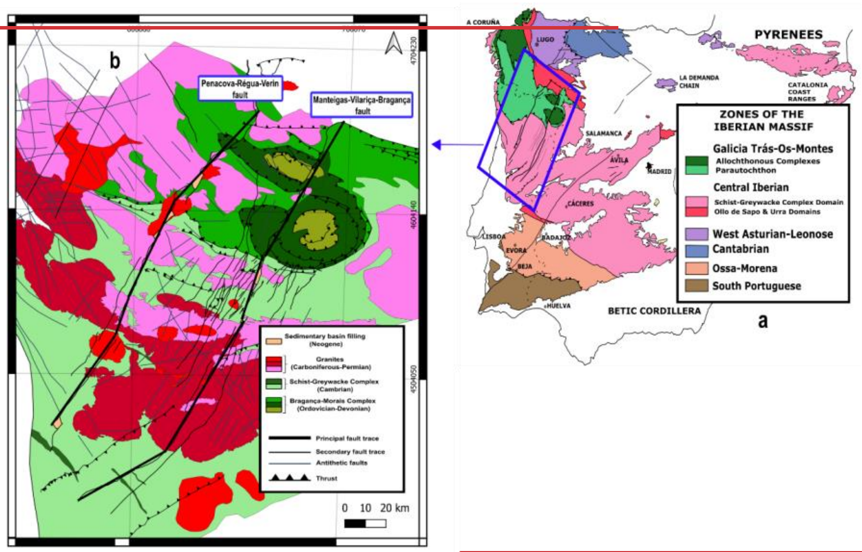

~~**Figure 8: a) Geological map of the Iberian Massif and the location of the natural example (modified from Martínez-Catalán, 2012 and Martín-González & Hereida, 2011). b) Schematic geological map of the NW of the Iberian Peninsula showing the main fault orientations at the different units. The antithetic faults are also represented following a NW-SE orientation.**~~

The PRV and MVB fault systems show different deformation patterns depending on the lithologies crossed like more parallel faults traces in the weak resistant units, or changes in the strike of the principal trace (Fig. 8). The pattern observed in the faults are comparable with our results in the analogue modelling experiments (e.g., models B1 and C1). The number of secondary fault traces are not the same. There is a greater number of secondary fault traces in the central section of the MVB fault, constituted essentially by slates that could be represented by the microbeads from models B2 and D2 (Panien et al., 2006). The region shows sinistral and antithetical faults mainly located in metamorphic units and granites respectively. The sinistral Penacova-Régua-Verin and Manteigas-Vilariça-Bragança faults are the main drivers for the recorded displacement, and the principal trace of both faults changes the strike after crosscut the lithologies with different rheology as in the models B1 and C1.

Con formato: Normal

5. Conclusions

Con formato: Esquema numerado + Nivel: 1 + Estilo de numeración: 1, 2, 3, … + Iniciar en: 1 + Alineación: Izquierda + Alineación: 0,63 cm + Sangría: 1,27 cm

This study evaluates the influence of vertical rheological contrasts using analogue models inspired by the deformation patterns of the strike-slip fault. Our study shows that the fault types and their evolution depend on the characteristic of the lithology and its contact orientation.

If the lithology is weak, in terms of low value of internal friction angle, the initial deformation is rather diffuse and thus difficult to see. In weak materials, localized deformation does not show up as fast as in stronger material; however, at the end they register a greater number of faults than the strong material.

The faults do not cut the rheological contrast if this is oriented oblique with respect to the shear direction, even though it is composed of weak material. The faults cut the contrast if this is oriented towards the shear direction, or when the contacts of the contrast are perpendicular to the shear direction and is composed by the weak material.

The initial fault's strike changes when they crosscut cut a new lithology. If the material is weak, the fault changes its initial strike clockwise. If the contrast is composed of the strong material, the initial fault strike changes anticlockwise.

We performed a series of analogue models to investigate faulting in the upper, brittle crust as a result of sinistral simple shear. The initial model had a rectangular shape with the long axis parallel to the shear direction. In two reference models, the brittle crust consisted of either a weak granular material (microbeads) or a strong granular material (quartz sand). In a further six models, we introduced mechanical strength contrasts in the upper crust, by introducing a vertical central domain consisting of quartz sand surrounded by microbeads (i.e. a weak-strong-weak configuration) or the other way around (i.e. a strong-weak-strong configuration). These models allowed us to test the influence of vertical domains of contrasting brittle strength on the fault pattern, and the influence of the weak-strong-weak and strong-weak-strong configuration.

- The fault pattern of models with a single granular material simulating the upper crust (i.e. no vertical domains of contrasting brittle mechanical strength) is dominated by sinistral (synthetic) strike-slip faulting, whose orientations are readily explained by the Mohr-Coulomb failure criterion, with fault strikes being a function of the internal friction angles, which differ between microbeads (ϕ=22°) and quartz sand (ϕ= 36°)
- In models with vertical domains of contrasting brittle strength, initial fault development occurs in the outer domains with syn-and antithetic faults forming in the expected orientations according to the Mohr-Coulomb failure criterion.
- In models with domains of contrasting brittle strength, the central domain boundaries are almost completely or fully activated if their strike orientation is subparallel to the predicted antithetic fault orientation. As a consequence, faulting occurs in three distinct structural domains.
- If the orientation of the domain boundaries is less favorably oriented, they are only partially activated or not at all, allowing synthetic faults that form in the outer domains to cut across the central domain. Hence, there are no distinct structural domains.
- If the central domain boundaries are fully activated and three structurally distinct domains form, the strength contrast between the domains (i.e. weak-strong-weak or strong-weak-strong) does not influence the overall fault pattern. However, if the domain boundaries remain inactive then the strength contrast between the domains has an influence on the fault development and evolution. In the case of weak-strong-weak, the synthetic faults from the outer domains cross-cut the central domain with a slight change in strike orientation, whereas in the case of strong-weak-strong, the weak central domain

show internal oblique-slip reverse faulting, which inhibits faults from the outer domain to fully cross the central domain.

- Although we only tested sinistral simple shear, our results can also be applied to dextral simple shear by mirroring the fault patterns around a N-S axis.
- Our results are comparable with the fault systems observed in the NW of the Iberian Peninsula. The faults The area shows synthetic and antithetic faults whose distribution is similar to the models made. In addition, refraction patterns of the main traces change their initial strike when they crosscut different geological units. The are a greater number of sinistral faults located in the weak units (slates). trace of the faults associated with lithological contrasts can be observed.

6. Competing interests

Con formato: Esquema numerado + Nivel: 1 + Estilo de numeración: 1, 2, 3, … + Iniciar en: 1 + Alineación: Izquierda + Alineación: 0,63 cm + Sangría: 1,27 cm

The contact author has declared that none of the authors has any competing interests.

7. Acknowledgments

Con formato: Esquema numerado + Nivel: 1 + Estilo de numeración: 1, 2, 3, … + Iniciar en: 1 + Alineación: Izquierda + Alineación: 0,63 cm + Sangría: 1,27 cm

The following work has been partially funded by a predoctoral contract (PREDOC20-073), by the Universidad Rey Juan Carlos and project PID2022-139527OB-I00 funded by MCIN/AEI/10.13039/501100011033/ and FEDER.

8. References

Con formato: Esquema numerado + Nivel: 1 + Estilo de numeración: 1, 2, 3, … + Iniciar en: 1 + Alineación: Izquierda + Alineación: 0,63 cm + Sangría: 1,27 cm

Alonso, J. L., Pulgar, J. A., García-Ramos, J. C., & Barba, P.: Tertiary basins and Alpine tectonics in the Cantabrian Mountains (NW Spain). in Tertiary Basins of Spain (pp. 214–227). Cambridge University Press. 1996

Aki, K.: Geometric features of a fault zone related to the nucleation and termination of an earthquake rupture, in: Proceedings of Conference XLV Fault Segmentation and Controls of Rupture Initiation and Termination. US Geological Survey Open File Report 89-315, pp. 1–9, 1989

Con formato: Francés (Suiza)

Arthaud, F., Matte, Ph.: Les decrochements tardi-hercyniens du sud-ouest de l'europe. Geometrie et essai de reconstitution des conditions de la deformation. Tectonophysics 25, 139–171. https://doi.org/10.1016/0040-1951(75)90014-1, 1975.

Anderson, E. M: The Dynamics of faulting and Dyke Formation with Applications to Britain (2nd edition), Oliver and Boyd, Edinburgh, Scotland, 1951.

Antonellini, M.A., Aydin, A., Pollard, D.D.: Microstructure of deformation bands in porous sandstones at Arches National Park, Utah. Journal of Structural Geology 16, 941e959, 1994.

Aydin, A., Nur, A.: Evolution of pull-apart basins and their scale independence. Tectonics 1, 91–105, 1982.

Aydin, A.: Fractures, faults, and hydrocarbon entrapment, migration and flow. Marine and Petroleum Geology 17, 797–814, 2000.

Aydin, A., & Berryman, J. G: Analysis of the growth of strike-slip faults using effective medium theory. *Journal of Structural Geology*, *32*(11), 1629–1642. https://doi.org/10.1016/j.jsg.2009.11.007, 2010.

Barka, A., Kadinsky-Cade, K.: Strike-slip fault geometry in Turkey and its influence on earthquake activity. Tectonics 7, 663–684, 1988.

Boutelier, D., Schrank, C., Regenauer-Lieb, K.: 2-D finite displacements and strain from particle imaging velocimetry (PIV) analysis of tectonic analogue models with TecPIV. Solid Earth 10, 1123-1139, 2019.

Burgmann, R., Pollard, D.D.: Strain accommodation about strike-slip fault discontinuities in granitic rock under brittle-to-ductile conditions. Journal of Structural Geology 16, 1655–1674, 1994.

Cazarin, C.L., van der Velde, R., Santos, R.V., Reijmer, J.J.G., Bezerra, F.H.R., Bertotti, G., La Bruna, V., Silva, D.C.C., de Castro, D.L., Srivastava, N.K., Barbosa, P. F.: Hydrothermal activity along a strike-slip fault zone and host units in the S˜ ao Francisco Craton, Brazil – implications for fluid flow in sedimentary basins. Precambrian Res. 365 https://doi.org/10.1016/j.precamres.2021.106365, 2021.

Cheng, X., Ding, W., Pan, L., Zou, Y., Li, Y., Yin, Y., & Ding, S.: Geometry and kinematics characteristics of strike-slip fault zone in complex structure area: A case study from the south no. 15 strike-slip fault zone in the Eastern Sichuan Basin, China. Frontiers in earth science, 10. https://doi.org/10.3389/feart.2022.922664, 2022.

Cooke, M. L., Toeneboehn, K., and Hatch, J. L.: Onset of slip partitioning under oblique convergence within scaled physical experiments, Geosphere, 16, 875-889. https ://doi.org/10.1130/GES02179.1, 2020.

de Joussineau, G., & Aydin, A.: Segmentation along strike-slip faults revisited. *Pure and Applied Geophysics*, *166*(10–11), 1575–1594. https://doi.org/10.1007/s00024-009-0511-4, 2009.

Deng, Q., Wu, D., Zhang, P., & Chen, S.: Structure and deformational character of strike-slip fault zones. Pure and Applied Geophysics, 124(1–2), 203–223. https://doi.org/10.1007/bf00875726, 1986.

Díez Fernández, R., Pereira, M.F.: Extensional orogenic collapse captured by strike-slip tectonics: Constraints from structural geology and UPb geochronology of the Pinhel shear zone (Variscan orogen, Iberian Massif). Tectonophysics 691, 290–310. https ://doi.org/10.1016/j.tecto.2016.10.023, 2016.

Dooley, T. P., & Schreurs, G. : Analogue modelling of intraplate strike-slip tectonics: A review and new experimental results. *Tectonophysics*, *574–575*, 1–71. https://doi.org/10.1016/j.tecto.2012.05.030, 2012

Du, Y., & Aydin, A.: Shear fracture patterns and connectivity at geometric complexities along strike-slip faults. *Journal of Geophysical Research*, *100*(B9), 18093–18102. https://doi.org/10.1029/95jb01574, 1995.

Fernández, M., Marzán, I., & Torne, M.: Lithospheric transition from the Variscan Iberian Massif to the Jurassic oceanic crust of the Central Atlantic. Tectonophysics, 386(1–2), 97–115. https://doi.org/10.1016/j.tecto.2004.05.005, 2004.

Gabrielsen, R. H., Giannenas, P. A., Sokoutis, D., Willingshofer, E., Hassaan, M., & Faleide, J. I.: Analogue experiments on releasing and restraining bends and their application to the study of the Barents Shear Margin. *Solid Earth*, *14*(9), 961–983. https://doi.org/10.5194/se-14-961-2023, 2023

Gamond, J.F.: Displacement features associated with fault zones: a comparison between observed examples and experimental models. Journal of Structural Geology 5, 33–45, 1983.

Con formato: Inglés (Estados Unidos)
Con formato: Inglés (Estados Unidos)
Con formato: Inglés (Estados Unidos)
Con formato: Inglés (Estados Unidos)
Con formato: Inglés (Estados Unidos)
Con formato: Inglés (Estados Unidos)

Garfunkel, Z., & Ron, H.: Block rotation and deformation by strike-slip faults: 2. The properties of a type of macroscopic discontinuous deformation. Journal of Geophysical Research, 90(B10), 8589–8602. https://doi.org/10.1029/jb090ib10p08589, 1985.

Gomes, A. S., Rosas, F. M., Duarte, J. C., Schellart, W. P., Almeida, J., Tomás, R., & Strak, V.: Analogue modelling of brittle shear zone propagation across upper crustal morpho-rheological heterogeneities. *Journal of Structural Geology*, *126*, 175–197. https://doi.org/10.1016/j.jsg.2019.06.004, 2019.

Gutiérrez-Alonso, G., Collins, A. S., Fernández-Suárez, J., Pastor-Galán, D., González-Clavijo, E., Jourdan, F., Weil, A. B., & Johnston, S. T.: Dating of lithospheric buckling: 40Ar/39Ar ages of syn-orocline strike–slip shear zones in northwestern Iberia. *Tectonophysics*, *643*, 44–54. https://doi.org/10.1016/j.tecto.2014.12.009, 2015.

Harris, R.A., Day, S.M.: Dynamic 3D simulation of earthquakes on en echelon faults. Geophysical Research Letters 26, 2089–2092, 1999.

Hubbert, M. K.: Theory of scale models as applied to the study of geologic structures. The Geological Society of America Bulletin, 48(10), 1459–1520. https://doi.org/10.1130/GSAB-48-1459, 1937.

Kavyani-Sadr, K., Rahimi, B., Khatib, M.M., Kim, Y.-S.: Assessment of open spaces related to Riedel-shears dip effect in brittle shear zones. J. Struct. Geol. 154, 104486 https://doi.org/10.1016/j.jsg.2021.104486, 2022.

Kim, Y., Peacock, D.C.P., Sanderson, D.J.: Fault damage zones. Journal of Structural Geology 26, 503–517, 2004.

Kirkland, C. L., Alsop, G. I., & Prave, A. R.: The brittle evolution of a major strike-slip fault associated with granite emplacement: a case study of the Leannan Fault, NW Ireland. Journal of the Geological Society, 165(1), 341–352. https://doi.org/10.1144/0016-76492007-064, 2008.

Lefevre, M., Souloumiac, P., Cubas, N., & Klinger, Y. : Experimental evidence for crustal control over seismic fault segmentation. Geology, 48(8), 844–848. https://doi.org/10.1130/g47115.1, 2020.

Livio, F. A., Ferrario, M. F., Frigerio, C., Zerboni, A., & Michetti, A. M.: Variable fault tip propagation rates affected by near-surface lithology and implications for fault displacement hazard assessment. Journal of Structural Geology, 130(103914), 103914. https://doi.org/10.1016/j.jsg.2019.103914, 2020.

Mair, K., Frye, K.M., Marone, C.: Influence of grain characteristics on the friction of granular shear zones. Journal of Geophysical Research 107 (B10), 4/1-4/9, 2002.

Matte, P.: Accretionary history and crustal evolution of the Variscan belt in Western Europe. *Tectonophysics*, *196*(3–4), 309–337. https://doi.org/10.1016/0040-1951(91)90328-p. 1991.

Martel, S.J., Peterson Jr., J.E.: Interdisciplinary characterization of fracture systems at the US/BK site, Grimsel Laboratory, Switzerland. International Journal of Rock Mechanics and Mining Science and Geomechanical Abstracts 28, 259–323, 1991.

Martínez Catalán, J. R., Arenas, R., Díaz García, F., & Abati, J.: Variscan accretionary complex of northwest Iberia: Terrane correlation and succession of tectonothermal events. *Geology*, *25*(12), 1103. https://doi.org/10.1130/0091-7613(1997)025<1103:vaconi>2.3.co;2. 1997

Martínez Catalán, J.R. : The Central Iberian arc, an orocline centered in the Iberian Massif and some implications for the Variscan belt. Int. J. Earth Sci. 101, 1299–1314. https://doi.org/10.1007/s00531-011-0715-6, 2012.

Martín-González, F., Heredia, N.: Geometry, structures and evolution of the western termination of the Alpine-Pyrenean Orogen reliefs (NW Iberian Peninsula). J. Iber. Geol. 37, 103–120. https://doi.org/10.5209/rev_JIGE.2011.v37.n2.1, 2011.

Martín-González, F., Barbero, L., Capote, R., Heredia, N., & Gallastegui, G.: Interaction of two successive Alpine deformation fronts: constraints from low-temperature thermochronology and structural mapping (NW Iberian Peninsula). *International Journal of Earth Sciences*, *101*(5), 1331–1342. https://doi.org/10.1007/s00531-011-0712-9. 2012.

Moore, J. D. P., & Parsons, B.: Scaling of viscous shear zones with depth-dependent viscosity and power-law stress–strain-rate dependence. *Geophysical Journal International*, *202*(1), 242–260. https://doi.org/10.1093/gji/ggv143, 2015.

Myers, R., Aydin, A.: The evolution of faults formed by shearing across joint zones in sandstone. Journal of Structural Geology 26, 947–966, 2004.

Con formato: Inglés (Estados Unidos)

Con formato: Sin subrayado, Color de fuente: Automático

Con formato: Inglés (Estados Unidos)

Con formato: Inglés (Estados Unidos)

Con formato: Alemán (Suiza)

Nicholson, C., Seeber, L., Williams, P. and Sykes, L.R.: Seismic evidence for conjugate slip and block rotation within the San Andreas fault system, Southern California. Tectonics, 5: 629-648, 1986

Odling, N.E., Harris, S.D., Knipe, R.J.: Permeability scaling properties of fault damage zones in siliclastic rocks. Journal of Structural Geology 26, 1727–1747, 2004.

Panien, M., Schreurs, G., & Pfiffner, A.: Mechanical behaviour of granular materials used in analogue modelling: insights from grain characterisation, ring-shear tests and analogue experiments. *Journal of Structural Geology*, *28*(9), 1710–1724. https://doi.org/10.1016/j.jsg.2006.05.004, 2006.

Peacock, D.C.P., Sanderson, D.J.: Displacement, segment linkage and relay ramps in normal fault zones. Journal of Structural Geology 13, 721–733, 1991.

Peacock, D. C. P., & Sanderson, D. J.: Effects of layering and anisotropy on fault geometry. *Journal of the Geological Society*, *149*(5), 793–802. https://doi.org/10.1144/gsjgs.149.5.0793, 1992.

Petersen, M. D., Dawson, T. E., Chen, R., Cao, T., Wills, C. J., Schwartz, D. P., & Frankel, A. D.: Fault displacement hazard for strike-slip faults. *Bulletin of the Seismological Society of America*, *101*(2), 805–825. https://doi.org/10.1785/0120100035, 2011.

Preuss, S., Herrendörfer, R., Gerya, T., Ampuero, J.-P., & Dinther, Y.: Seismic and aseismic fault growth lead to different fault orientations. Journal of Geophysical Research. Solid Earth, 124(8), 8867–8889. https://doi.org/10.1029/2019jb017324, 2019.

Ramberg, H.: Gravity, deformation and the Earth's crust: In theory, experiments and geological application (p. 452). Academic Press, 1981.

Richard, P.: Experiments on faulting in a two-layered cover sequence overlying a reactivated basement fault with oblique-slip. J. Struct. Geol. 13, 459–469, 1991.

Richard, P., Naylor, M.A., Koopman, A.: Experimental models of strike-slip tectonics. Petroleum Geoscience 1, 71–80, 1995.

Rispoli, R.: Stress fields about strike-slip faults inferred from stylolites and tension gashes. Tectonophysics 75, 729–736, 1981.

Ron, H., Freund, R., Garfunkel, Z. and Nur, A.: Block rotation by strike slip faulting: structural and paleomagnetic evidence. J. Geophys. Res., 89: 6256-6270, 1984.

Schellart, W.P., Strak, V.: A review of analogue modelling of geodynamic processes: Approaches, scaling, materials and quantification, with an application to subduction experiments. J. Geodyn. 100, 7–32. https://doi.org/10.1016/j. jog.2016.03.009, 2016.

Schmid, T., Schreurs, G. Warsitzka, M., & Rosenau, M.: Effect of sieving height on density and friction of brittle analogue material: Ring-shear test data of quartz sand used for analogue experiments in the Tectonic Modelling Lab of the University of Bern. GFZ Data Services. https://doi.org/10.5880/fidgeo.2020.006, 2020.

Schmid, T. C., Schreurs, G., & Adam, J.: Rotational extension promotes coeval upper crustal brittle faulting and deep-seated rift-axis parallel flow: Dynamic coupling processes inferred from analog model experiments. *Journal of Geophysical Research. Solid Earth*, *127*(8). https://doi.org/10.1029/2022jb024434, 2022.

~~Schmid, T. C., Brune, S., Glerum, A., & Schreurs, G.: *Tectonic interactions during rift linkage: Insights from analog and numerical experiments*. https://doi.org/10.5194/egusphere-2022-1203, 2023~~

Scholz, C. H.: *The Mechanics of Earthquakes and Faulting*. Cambridge University Press, 2002.

Segall, P., & Pollard, D. D.: Nucleation and growth of strike slip faults in granite. *Journal of Geophysical Research*, *88*(B1), 555. https://doi.org/10.1029/jb088ib01p00555, 1983.

Shaw, B.E., Dieterich, J.H.: Probabilities for jumping fault segment stepovers. Geophysical Research Letters 34, L01307. doi:10.1029/2006GL027980, 2007.

Sibson, R.H.: Stopping of earthquake ruptures at dilational fault jogs. Nature 316, 248–251, 1985.

Stirling, M.W., Wesnousky, S.G., Shimazaki, K.: Fault trace complexity, cumulative slip, and the shape of the magnitude-frequency distribution for strike-slip faults: a global survey. Geophysical Journal International 124, 833–868, 1996.

Sylvester, A.G.: Strike-slip faults. Geol. Soc. Am. Bull. 100, 1666–1703. https:// doi.org/10.1130/0016-7606(1988)1002.3.CO;2, 1988.

Vegas, R., Vicente Muñoz, G., Muñoz Martín, A., & Palomino, R..: *Los corredores de fallas de Régua-Verin y Vilariça: Zonas de transferencia de la deformación intraplaca en la Península Ibérica*. 2004

Veludo, I., Dias, N. A., Fonseca, P. E., Matias, L., Carrilho, F., Haberland, C., & Villaseñor, A.: Crustal seismic structure beneath Portugal and southern Galicia (Western Iberia) and the role of Variscan inheritance. Tectonophysics, 717, 645–664. https://doi.org/10.1016/j.tecto.2017.08.018. 2017

Venâncio, M. B., & da Silva, F. C. A.: Structures evolution along strike-slip fault zones: The role of rheology revealed by PIV analysis of analog modeling. Tectonophysics, 229764, 229764. https://doi.org/10.1016/j.tecto.2023.229764, 2023.

Vergés, J., Kullberg, J. C., Casas-Sainz, A., de Vicente, G., Duarte, L. V., Fernàndez, M., Gómez, J. J., Gómez-Pugnaire, M. T., Jabaloy Sánchez, A., López-Gómez, J., Macchiavelli, C., Martín-Algarra, A., Martín-Chivelet, J., Muñoz, J. A., Quesada, C., Terrinha, P., Torné, M., & Vegas, R.: An introduction to the alpine cycle in Iberia. En The Geology of Iberia: A Geodynamic Approach (pp. 1–14). Springer International Publishing. 2019

Viola, G., Odonne, F., Mancktelow, N.S.: Analogue modelling of reverse fault reactivation in strike–slip and transpressive regimes: application to the Giudicarie fault system, Italian Eastern Alps. J. Struct. Geol. 36, 401–418. https://doi.org/ 10.1016/j.jsg.2003.08.014, 2004.

Wesnousky, S.G.: Seismological and structural evolution of strike-slip faults. Nature 335, 340–342, 1988.

Wesnousky, S.G.: Predicting the endpoints of earthquake ruptures. Nature 444, 358–360, 2006.

Westerweel, J., Scarano, F.: Universal outlier detection for PIV data. Experiments in fluids 39, 1096-1100, 2005.

Zwaan, F., Schreurs, G., Ritter, M., Santimano, T., & Rosenau, M.: Rheology of PDMS-corundum sand mixtures from the Tectonic Modelling Lab of the University of Bern (CH). V. 1. GFZ data Services. https://doi. org/10.5880/fdgeo.2018.023, ~~2018e~~2018.

Zwaan, F., Schreurs, G., Gentzmann, R., Warsitzka, M. & Rosenau, M. Ring-shear test data of quartz sand from the Tectonic Modelling Lab of the University of Bern (CH). GFZ Data Services, http://doi.org/10.5880/fidgeo.2018.028

Zwaan, F., Schreurs, G., Madritsch, H., & Herwegh, M.: Influence of rheologically weak layers on fault architecture: insights from analogue models in the context of the Northern Alpine Foreland Basin. Swiss Journal of Geosciences, 115(1). https://doi.org/10.1186/s00015-022-00427-8, 2022.

Con formato: Inglés (Estados Unidos)

Con formato: Inglés (Estados Unidos)

Con formato: Inglés (Estados Unidos)

Con formato: Inglés (Estados Unidos)

Con formato: Inglés (Estados Unidos)

Con formato: Fuente: +Cuerpo (Calibri), 11 pto, Inglés (Reino Unido)